Crustal Anisotropy Across Eastern Tibet and Surroundings Modeled as a Depth-Dependent Tilted Hexagonally Symmetric Medium

Crustal Anisotropy Across Eastern Tibet and Surroundings Modeled as a Depth-Dependent Tilted Hexagonally Symmetric Medium

Jiayi Xie[1], Michael H. Ritzwoller[1], W. Shen[1,2], Weitao Wang[3]

1- Department of Physics, University of Colorado at Boulder, Boulder, CO 80309, USA
jiayi.xie@colorado.edu
2 – now at Department of Earth and Planetary Sciences, Washington University, St. Louis, MO 63130
3 - Institute of Geophysics, Chinese Earthquake Administration, Beijing 100045 China

Abstract

Two types of surface wave anisotropy are observed regularly by seismologists but are only rarely interpreted jointly: apparent radial anisotropy, which is the difference in propagation speed between horizontally and vertically polarized waves inferred from Love and Rayleigh waves, and apparent azimuthal anisotropy, which is the directional dependence of surface wave speeds (usually Rayleigh waves). We show that a new data set of Love and Rayleigh wave isotropic phase speeds and Rayleigh wave azimuthal anisotropy observed within and surrounding eastern Tibet can be explained simultaneously by modeling the crust as a depth-dependent tilted hexagonally symmetric (THS) medium. We specify the THS medium with depth-dependent hexagonally symmetric elastic tensors tilted and rotated through dip and strike angles and estimate these quantities using a Bayesian Monte Carlo inversion to produce a 3-D model of the crust and uppermost mantle on a 0.5°x0.5° spatial grid. In the interior of eastern Tibet and in the Yunnan-Guizhou plateau, we infer a steeply dipping THS upper crustal medium overlying a shallowly dipping THS medium in the middle-to-lower crust. Such vertical stratification of anisotropy may reflect a brittle to ductile transition in which shallow fractures and faults control upper crustal anisotropy and the crystal preferred orientation of anisotropic (perhaps micaceous) minerals governs the anisotropy of the deeper crust. In contrast, near the periphery of the Tibetan Plateau the anisotropic medium is steeply dipping throughout the entire crust, which may be caused by the reorientation of the symmetry axes of deeper crustal anisotropic minerals as crustal flows are rotated near the borders of Tibet.

1. Introduction

The high Tibetan Plateau has resulted from the collision of India with Eurasia over the past 45 million years [*Molnar and Tapponnier*, 1975; *Jolivet et al.*, 1990; *Le Fort*, 1975]. How the plateau has deformed in response to the collision and how it has deformed surrounding regions remains subject to debate, and has inspired a wide range of tectonic models. Hypotheses have included deformation via rigid blocks [e.g., *Tapponnier et al.*, 2001], the continuous deformation of the entire lithosphere [e.g., *Molnar and Tapponnier*, 1975; *Houseman and England*, 1993], and flow in the lower crust [e.g., *Royden et al.*, 1997].

As suggested by heat flow measurements [*Francheteau et al.*, 1984] and thermo-kinematic models [*Bollinger et al.*, 2006], the thickened Tibetan crust is believed to be hot, which implies a significant weakness of the middle and lower crust [*Francheteau et al.*, 1984; *Nelson et al.*, 1996; *Clark and Royden*, 2000; *Beaumont et al.*, 2001]. In addition, earthquakes are mainly confined to the upper crust of Tibet where brittle deformation occurs [e.g., *Chu et al.*, 2009; *Zhang et al.*, 2010; *Sloan et al.*, 2011], seismic tomography has identified low velocity zones in the middle to lower crust [e.g., *Yao et al.*, 2008; *Yang et al.*, 2012; *Xie et al.*, 2013], and receiver function studies observe velocity jumps in the middle crust [e.g., *Kind et al.*, 2002; *Nabelek et al.*, 2009; *Li et al.*, 2011; *Deng et al.*, 2015]. Some researchers take these results as evidence for a viscously deforming deeper crust [e.g., *Clark and Royden*, 2000; *Beaumont et al.*, 2001], which may imply a decoupling between the upper crust and the underlying mantle. Partial melt in the middle crust may also be a common feature of central Tibet [e.g., *Hacker et al.*, 2014]. On the other hand, some authors argue that the Tibetan lithosphere is deforming as a coherent unit [e.g., *England and Molnar*, 1997], at least in southern Tibet [*Copley et al.*, 2011].

In this paper, we investigate the state of the upper and middle-to-lower crust of Tibet based on inferences about seismic anisotropy. There have been a number of previous studies of crustal anisotropy across Tibet based on surface waves from ambient noise or earthquake data. Radial anisotropy is the difference in propagation speed between horizontally and vertically polarized waves, inferred from Love and Rayleigh waves, respectively. Crustal radial anisotropy has been mapped across parts of Tibet by, for example, *Shapiro et al.* [2004], *Chen et al.* [2009], *Huang et al.* [2010], *Duret et al.* [2010], *Guo et al.* [2012], *Xie et al.* [2013], *Agius and Lebedev* [2014], and *Tan et al.* [2015]. Azimuthal anisotropy characterizes how propagation speed varies with azimuth. The Rayleigh wave azimuthal anisotropy of the crust also has been mapped by *Wei et al.* [2008], *Yao et al.* [2010], and *Pandey et al.* [2015].

The novelty of the current study lies in its simultaneous interpretation of observations of radial and azimuthal anisotropy from surface waves by estimating the depth-dependent oriented elastic tensor in the crust. *Xie et al.* [2015], influenced by much earlier studies of *Montagner and Nataf* [1986, 1988] *and Montagner and Jobert* [1988], presents a method to infer the oriented elastic tensor from such observations by imposing the constraint that the elastic tensor possesses hexagonal symmetry with an orientation (described by dip and strike angles, **Fig. 1**) that is constant throughout the crust. They conclude that only one dip angle (and strike angle) is needed at each location across the relatively thin crust that composes the western US. However, the Tibetan crust is much thicker and many studies have observed significant vertical complications in crustal structure, such as a significant mid-crustal discontinuities [e.g., *Kind et al.*, 2002; *Nábě lek et al.*, 2009; *Li et al.*, 2011; *Deng et al.,* 2015] and crustal low velocity zones [e.g., *Kind et al.*, 1996; *Cotte et al.*, 1999; *Rapine et al.*, 2003; *Shapiro et al.*, 2004; *Xu et al.*, 2007; *Yao et al.*, 2008; *Caldwell et al.*, 2009; *Guo et al.*, 2009; *Li et al.*, 2009; *Acton et al.*, 2010; *Jiang et al.*,

2011; *Xie et al.*, 2013; *Deng et al.,* 2015]. Here, we consider the effects that such complications might have on the inference of the oriented elastic tensor across eastern Tibet and adjacent regions.

Estimating the oriented elastic tensor interests us because it may provide insight into the geometry of foliation of material that composes the Tibetan crust, which may provide new constraints on deformation. In particular, estimates of the elastic tensor for the crust of Tibet may provide new information about the difference or similarity between the Tibetan upper and middle-to-lower crust.

In discussing anisotropy it is important to keep in mind two different coordinate frames (**Fig. 1**): the frame in which the observations are made and the frame defined by the symmetry axis of the medium. We define the elastic tensor in the coordinate frame of the medium (x_1,x_2,x_3), in which the 3-axis aligns with the symmetry axis and the coordinate pair (x_1,x_2) spans the foliation plane. We refer to anisotropy defined in this frame as "*inherent*". In this frame, a hexagonally symmetric medium possesses no azimuthal anisotropy, where azimuth is defined in terms of rotation about the symmetry axis. In contrast, the coordinate system of observation is represented by the three-components of seismometers at the Earth's surface ($\hat{x}_1,\hat{x}_2,\hat{x}_3$) in which the 3-axis lies normal to the Earth's surface. In this frame, observations of anisotropy depend on how the components of the elastic tensor, composed of the inherent elastic moduli, are affected by the tilt of the medium (or the rotation of the symmetry axis). We refer to measurements of anisotropy and inferences drawn from them in the observational frame as "*apparent*". Most studies of anisotropy based on surface waves have reported measurements and models of particular aspects of apparent anisotropy, such as radial and azimuthal anisotropy. In particular, azimuthal

anisotropy is a commonly observed property.

The purpose of this paper is to address the following questions with a focus on eastern Tibet and surrounding areas: (1) First, can information about anisotropy contained in surface wave travel times observed across Tibet be fit with the oriented elastic tensor model, in the same way as similar data were fit in the western US by *Xie et al.* [2015]? (2) Second, is there a difference in anisotropy between the upper crust and middle-to-lower crust across Tibet? Specifically, is a single orientation for the elastic tensor at all depths in the crust sufficient to fit the observations? (3) Finally, does the nature and vertical distribution of anisotropy across Tibet differ from that across surrounding regions?

In order to address these questions, we combine data from three networks across parts of China and Tibet: the China Earthquake Array (CEArray), the China Array deployed in and around Yunnan Province, and the PASSCAL installations in Tibet (**Fig. 2b**). Based on recordings from these stations we obtain Rayleigh and Love wave phase velocity measurements from ambient noise by assimilating phase velocity measurements from previous studies and also updating Love wave phase velocity maps by introducing new observations. Rayleigh wave phase velocity maps for Tibet were previously presented by *Yang et al.* [2012], *Xie et al.* [2013] and later by *Shen et al.* [2016] who produced an isotropic and azimuthally anisotropic data set of observed surface wave phase speeds from ambient noise that covers most of China. These studies ultimately yield an integrated data set of Rayleigh wave phase speed measurements and maps, which we incorporate here. The new measurements we incorporate include both the isotropic and azimuthally anisotropic components of Rayleigh wave phase speeds (**Fig. 3**). *Xie et al* [2013] present isotropic Love wave phase speed maps for Tibet. Here, we add new measurements of Love wave phase speeds based on ambient noise recorded at 438 China Array stations in and

around Yunnan Province, and produce updated Love wave phase speed maps.

The remainder of this paper is separated into five principal sections. In section 2, we briefly describe the data used in our inversion, which is period-dependent surface wave phase speeds extracted from Rayleigh and Love wave tomography, including data sensitivity and uncertainties. In section 3, we clarify the terminology and concepts that underlie our work, particularly as related to the notions of inherent and apparent anisotropy. In section 4 we describe the model parameterization and constraints applied in the Bayesian Monte Carlo inversion. In section 5, we describe the model of the depth-dependent tilted elastic tensor in the crust that explains this data set and present views with horizontal maps and vertical profiles of the estimated dip and inherent strength of anisotropy and their uncertainties. In section 6, we provide views of apparent anisotropy to aid comparison with previous studies and discuss the physical and geological significance of the results.

2. Data

2.1 Measurements

In this study, we combine new ambient noise based Love wave phase velocity measurements with previously observed Rayleigh and Love wave phase speed measurements obtained from cross-correlations of continuous ambient noise data. First, for Rayleigh waves, we incorporate the subset of the maps of isotropic and azimuthally anisotropy phase velocities from *Shen et al.* [2016] that covers our study area. *Shen et al.* [2016] produce isotropic Rayleigh wave phase speed maps (8 to 50 sec period) using ray theoretic tomography [*Barmin et al.*, 2001], and simultaneously estimate maps of azimuthal anisotropy. Second, we also incorporate the isotropic Love wave phase speed measurements obtained by *Xie et al.* [2013] using ambient noise cross-correlations based on CEArray and PASSCAL data. Finally, we introduce new Love wave phase speed measurements obtained from cross-correlations of ambient noise recorded at the 438 China Array stations centered on Yunnan Province. The Love wave phase velocity measurements for each cross-correlation station pair are measured using automated frequency-time analysis (FTAN) [*Levshin and Ritzwoller*, 2001; *Bensen et al.*, 2007] as in the study of *Xie et al.* [2013]. We apply ray theoretic tomography [*Barmin et al.*, 2001] to generate azimuthally variable and isotropic Love wave phase velocity maps from 8 to 40 sec period. As described below, we only interpret the isotropic component of the resulting Love wave maps here.

In a weakly anisotropic medium, the azimuthal dependence of phase velocity for a Rayleigh wave has the following form [*Smith and Dahlen*, 1973]:

$$c(T, \psi) = c_0(T)[1 + a_2 \cos\big(2(\psi - \varphi_{FA})\big) + a_4 \cos\big(4(\psi - \alpha)\big)] \qquad (1)$$

where T is period, ψ is the azimuth of propagation of the wave measured clockwise from north, $c_0(T)$ is the isotropic phase speed, φ_{FA} is the 2ψ fast axis orientation, α is an analogous angle for the 4ψ variation in phase velocity, and a_2 and a_4 are the relative amplitudes of the 2ψ and 4ψ anisotropy. Based on theoretical arguments [*Smith and Dahlen*, 1973; *Montagner and Nataf*, 1986] and observations [e.g., *Lin and Ritzwoller*, 2011; *Lin et al.*, 2011; *Xie et al.*, 2015], the 2ψ term (180° periodicity) is understood to dominate the Rayleigh wave azimuthal variation, so we will only present the 2ψ signal here for Rayleigh waves. However, Love wave azimuthal anisotropy is dominated by the 4ψ term (90° periodicity), which means that exceptionally good azimuthal coverage is required for Love wave anisotropy to be measured reliably. Because the azimuthal coverage is not ideal across much of Tibet and because Love wave observations are typically noisier than Rayleigh wave observations, we do not use the azimuthal anisotropy observed for Love waves in the inversion presented here. The observations of Love wave azimuthal anisotropy help to insure that the isotropic Love wave phase speeds are not biased by azimuthal anisotropy.

We produce isotropic phase speed maps for Love waves (8 to 40 sec period) and Rayleigh waves (8 to 50 sec period), and 2ψ azimuthal anisotropy maps for Rayleigh waves (8 to 50 sec period). The difference between the isotropic parts of Love and Rayleigh wave phase speeds is shown in **Figure 3a,b** at periods of 10 sec and 30 sec. Love wave phase speeds are everywhere faster than Rayleigh wave speeds in the period band of measurement, but the difference between Love and Rayleigh wave speeds (referred to as $C_{Love} - C_{Rayleigh}$ in **Fig. 3**) depends on period and location. Examples of Rayleigh wave azimuthally anisotropic phase velocity maps are presented in **Figure 3c,d** at 10 sec and 30 sec period, where the length of each bar is the amplitude of 2ψ anisotropy (a_2 in equation 1, in percent), and the orientation of each bar is the fast-axis orientation (φ_{FA} in

equation 1). The azimuthal anisotropy has large amplitudes within Tibet and in the Yunnan-Guizhou plateau south of the Sichuan basin. At short periods, fast axis directions generally follow the orientations of surface faults.

2.2 Data sensitivity

The differences between Love and Rayleigh wave phase speeds shown in **Figure 3a,b** reflect the amplitude of the Rayleigh-Love discrepancy in our observations and provide information about the depth distribution of S-wave anisotropy. The Rayleigh-Love discrepancy is a measure of the inability of a simply parameterized isotropic model to fit Rayleigh and Love wave dispersion curves simultaneously. The introduction of radial anisotropy, or the speed difference between horizontally polarized (V_{SH}) and vertically polarized (V_{SV}) waves in a transversely isotropic medium (TI) (hexagonally symmetric medium with a vertical symmetry axis), is one way to resolve the Rayleigh-Love discrepancy. In general, the phase speed difference between Love and Rayleigh waves increases within the eastern Tibetan Plateau up to about a period of 30 s, and decreases or remains nearly constant with period outside of the Plateau. Procedurally, we specify anisotropy with the elastic tensor and its orientation, and use the notation V_{PV}, V_{PH}, V_{SH}, and V_{SV} only when speaking of a TI medium. In a medium with a tilted symmetry axis, we will specify anisotropy exclusively in terms of the Love moduli A, C, N, L, and F.

Synthetic examples of the difference between Love and Rayleigh wave phase speeds are shown in **Figure 4a,b**. Four models of the depth distribution of the difference between Vsh and Vsv in a TI medium are shown in **Figure 4a** and the resulting differences between Love and Rayleigh wave phase speeds ($C_{Love} - C_{Rayleigh}$) are shown in **Figure 4b**, which depend strongly on the amplitude and depth distribution of the difference V_{SH} - V_{SV}. For example, comparing the two

models in which one is isotropic (green line, **Fig. 4a**) and the other has a depth constant radial anisotropy ($V_{SH} - V_{SV} = 5\%$, black line, **Fig. 4b**) in the crust, there is a difference in C_{Love} - $C_{Rayleigh}$ of more than 200 m/s, which is a very large effect. The concentration of radial anisotropy in progressively narrower and deeper depth ranges in the crust has a progressively decreasing effect on the Love – Rayleigh phase speed difference. The shapes of the curves in **Figure 4b** depend on several factors. The period of the peak difference between Love and Rayleigh wave phase speeds depends largely on crustal thickness. The negative slope of the curves at periods longer than the peak period occurs because the Rayleigh wave becomes sensitive to the mantle at shorter periods than the Love wave. The upward curve at long periods occurs because of increasing sensitivity of Love waves to mantle anisotropy.

As discussed further in section 3, a TI medium can be characterized with five elastic moduli. Rayleigh and Love waves are differentially sensitive to these five moduli, which can be represented with the Love parameters A, C, N, L, and F or Vsv, Vsh, Vpv, Vph, and η. As **Figure 4c,d** illustrates, Rayleigh waves are predominantly sensitive to Vsv and Love waves are almost entirely sensitive to Vsh. Rayleigh waves also possess substantial sensitivity to η and to both Vpv and Vph, although the Vpv and Vph sensitivities tend to cancel one another which results in a sensitivity to Vpv that is much weaker and more shallow than to V_{SV}. Love waves are sensitive to shallower structures than Rayleigh waves at a given period, the effect of which is amplified in this study because our Love wave measurements only extend up to 40 s period whereas the Rayleigh waves extend to 50 s. The sensitivity kernels in **Figure 4c,d** are at the longest periods of this study. Love wave phase speed sensitivity at 40 s period extends only to about 50 km depth (at 25% of the maximum amplitude of the sensitivity curve) whereas Rayleigh wave sensitivity at 50 s period extends to greater than 100 km (based on the same

relative amplitude criterion). This difference in depth sensitivity of Love and Rayleigh waves has

implications for the reliability of estimates of anisotropy, as discussed in section 6.3.1.

In the inversion for the elastic tensor the differential sensitivity of Rayleigh and Love waves to

the elastic moduli allows only some of the moduli to be estimated well. This is complicated

further by the need to estimate the dip and rotation angles for the elastic tensor. Much of the

point of the Bayesian Monte Carlo inversion procedure described later is to estimate the relative

precision with which the different moduli and rotation angles can be estimated.

2.3 Uncertainty estimates

Because eikonal tomography [*Lin et al.*, 2009] models off great circle propagation and provides

an estimate of uncertainty, everything else being equal we would prefer to use it rather than the

traditional ray theoretic tomography that we apply here [*Barmin et al.*, 2001]. However, eikonal

tomography does not perform well in the presence of spatial gaps in the station coverage such as

those found in eastern Tibet. Such spatial gaps prevent us from constructing accurate phase

velocity maps and uncertainty estimates using eikonal tomography across much of the study

region. Thus, our uncertainty estimates for the isotropic phase velocity maps (Love and Rayleigh

waves) and azimuthal anisotropy maps (Rayleigh wave) are based on the spatially averaged 1σ

uncertainty estimates obtained by applying eikonal tomography where the method does work in

the region of study. Where eikonal tomography does not work well we scale up the spatially

averaged uncertainty. To do this we are motivated by the procedure described at greater length

by *Shen et al.* [2016]. We scale the measurement uncertainties based on some combination of

three factors: resolution, ray-path azimuthal coverage, and the amplitude of azimuthal

anisotropy. The uncertainties for Rayleigh and Love wave isotropic phase speed maps are scaled

using resolution alone as a guide, as described by *Shen et al* [2016]. The uncertainty for Rayleigh

wave azimuthal anisotropy amplitude is scaled using both resolution and azimuthal coverage.

Uncertainty for the Rayleigh wave azimuthal anisotropy fast axis is scaled using all three factors.

Examples of uncertainties in measured quantities are presented as one standard deviation error

bars in **Figure 5**.

2.4 Dispersion curves

From the Love wave (8 – 40 s period) and Rayleigh wave (8 – 50 s period) isotropic phase speed

maps, the Rayleigh wave azimuthal anisotropy maps, and their uncertainties, we generate at all

locations on a 0.5°×0.5° grid across the study region isotropic phase speed curves for both

Rayleigh and Love waves and period-dependent curves of the amplitude and fast axis orientation

of Rayleigh wave azimuthal anisotropy. These four local curves form the basis for the 3-D model

inversion described later in the paper.

Figure 5 presents examples of these local dispersion curves at the four locations identified in the

Figure 2a (A: eastern Tibet, B: Qilian terrane, C: Chuandian terrane just off the Tibetan plateau,

E: Yunnan-Guizhou plateau). Instead of showing the Love and Rayleigh wave isotropic phase

speed curves separately, we present the difference between them as in the simulation results

presented in **Figure 4b**, although in the inversion they are used as two independent observations.

Phase speed differences are presented as error bars, defined as the quadratic sum of the estimated

uncertainties of the Rayleigh and Love wave phase speeds at each location. As shown in **Figure

5a**, within Tibet the difference between Love and Rayleigh wave phase speeds increases rapidly

to peak at about 30 s and decreases slowly at longer periods. Outside of Tibet (**Fig. 5d,g,j**) the

difference increases at short periods less rapidly than in Tibet, peaks at a shorter period, and then

decreases either quicker or remains flat with period. A comparison of the synthetic curves in

Figure 4b with the observations in **Figures 5a,d,g,j** provides hints to the depth distribution of

radial anisotropy in Tibet and regions surrounding it.

In addition, the middle and bottom rows of **Figure 5** show the period dependent curves for the

amplitude and fast axis orientation of Rayleigh wave 2ψ azimuthal anisotropy, respectively. The

features of these curves vary dramatically from place to place. For example, at Point A (eastern

Tibet), the amplitude of Rayleigh wave azimuthal anisotropy decreases with period and the

Rayleigh wave fast azimuth does not change strongly with period. In contrast, at Point B (Qilian

terrane), the amplitude of Rayleigh wave azimuthal anisotropy remains flat with period but the

Rayleigh wave fast azimuth decreases moderately with period. At Points C and D, azimuthal

anisotropy changes in still different ways with period. At Point C the amplitude of anisotropy

increases with period and at Point D the fast axis orientation differs appreciably between short

and long periods, which indicates a change in the orientation of anisotropy with depth.

3. Background: Terminology for a Hexagonally Symmetric Medium

The spatially dependent isotropic and azimuthally anisotropic phase velocity measurements

described above provide information about the isotropic and anisotropic properties of the crust

and uppermost mantle. The properties of an elastic medium and seismic wave velocities depend

on the depth-dependent constitution and orientation of the elastic tensor, which consists of 21

independent components for a general anisotropic medium. Simplifications are needed in order

to constrain aspects of the elastic tensor. A useful starting point is the assumption that the

medium possesses hexagonal symmetry, which at each depth is described by five unique elastic

moduli known as the Love moduli: A, C, N, L, F [*Montagner and Nataf*, 1988; *Xie et al.*, 2015].

A and C are compressional moduli and N and L are shear moduli. The Voigt simplification of the elastic tensor is the 6x6 elastic modulus matrix, $C_{\alpha\beta}$, which for a hexagonally symmetric medium with a vertical symmetry axis is given by:

$$^{V}C_{\alpha\beta} = \begin{bmatrix} A & A-2N & F & 0 & 0 & 0 \\ A-2N & A & F & 0 & 0 & 0 \\ F & F & C & 0 & 0 & 0 \\ 0 & 0 & 0 & L & 0 & 0 \\ 0 & 0 & 0 & 0 & L & 0 \\ 0 & 0 & 0 & 0 & 0 & N \end{bmatrix} \tag{2}$$

where the V superscript denotes "vertical" for the orientation of the symmetry axis. With a vertical symmetry axis, a hexagonally symmetric medium will produce no azimuthal variation is surface wave speeds. A hexagonally symmetric medium may possess either a slow or fast symmetry axis; the slow symmetry case occurs when C < A and L < N, which crustal rocks generally display and finely layered media require [e.g. *Brownlee et al.*, 2011*; Erdman et al.*, 2013*; Thomsen and Anderson*, 2015]. Fast symmetry implies that C > A and L > N.

A hexagonally symmetric medium with a vertical symmetry axis (transversely isotropic, TI) is unique in that the 3-axis of the medium coordinates (symmetry axis) coincides with the 3-axis of the observing coordinates (vertical direction), as defined in **Figure 1**. For a TI medium, four of the five Love moduli are directly related to P and S wave speeds for waves propagating vertically or horizontally in the Earth: A = ρV^2_{PH}, C = ρV^2_{PV}, L = ρV^2_{SV}, N = ρV^2_{SH}.. Here ρ is density, V_{PH} and V_{PV} are the speeds of P waves propagating horizontally and vertically in the Earth, V_{SV} is the speed of the S wave propagating horizontally and polarized vertically or propagating vertically and polarized horizontally, and V_{SH} is the speed of the S wave that is propagating in a horizontal direction and polarized horizontally. The modulus $F = \eta(A - 2L)$ affects the speed of waves propagating

oblique to the symmetry axis and controls the shape of the shear wave phase speed surface [*Okaya and Christensen,* 2002]. For an isotropic medium, $A = C, L = N, F = A - 2L, \eta = 1$.

Hexagonally symmetric earth media may have a non-vertical, tilted and rotated symmetry axis as illustrated in **Figure 1**, where the tilt is denoted by the dip angle θ and the rotation by the strike angle ϕ. We use the notation V_{PH}, V_{PV}, V_{SV}, and V_{SH} only when discussing a medium with a vertical symmetry axis or an isotropic medium. With a tilted symmetry axis, we will use the notation A, C, N, L, and F (or $\eta = F/(A\text{-}2L)$) to represent the elements of the elastic tensor. We also introduce the following terminology: VHS for a hexagonally symmetric medium with a vertical symmetry axis, HHS for a hexagonally symmetric medium with a horizontal symmetry axis and THS for a hexagonally symmetric medium with a tilted symmetry axis.

A rotation of the medium will rotate the elastic tensor in equation (2) to produce the modulus matrix $C_{\alpha\beta}(\theta,\phi)$. We refer to a general reorientation of the symmetry axis as a tilt, which is achieved by pre- and post-multiplying the elastic modulus matrix by the appropriate rotation matrix and its transpose, respectively [e.g, *Auld*, 1973; *Carcione*, 2007], which act to rotate the 4th-order elasticity tensor appropriately. The rotation can fill all components of the modulus matrix but will preserve its symmetry:

$$C_{\alpha\beta}(\theta,\phi) = \begin{bmatrix} C_{11} & C_{12} & C_{13} & C_{14} & C_{15} & C_{16} \\ C_{12} & C_{22} & C_{23} & C_{24} & C_{25} & C_{26} \\ C_{13} & C_{23} & C_{33} & C_{34} & C_{35} & C_{36} \\ C_{14} & C_{24} & C_{34} & C_{44} & C_{45} & C_{46} \\ C_{15} & C_{25} & C_{35} & C_{45} & C_{55} & C_{56} \\ C_{16} & C_{26} & C_{36} & C_{46} & C_{56} & C_{66} \end{bmatrix} \tag{3}$$

Montagner and Nataf [1986] showed that this modulus matrix may be decomposed into

azimuthally independent and azimuthally dependent parts as follows:

$$
C_{\alpha\beta}(\theta,\phi) =
\begin{bmatrix}
\hat{A} & \hat{A}-2\hat{N} & \hat{F} & 0 & 0 & 0 \\
\hat{A}-2\hat{N} & \hat{A} & \hat{F} & 0 & 0 & 0 \\
\hat{F} & \hat{F} & \hat{C} & 0 & 0 & 0 \\
0 & 0 & 0 & \hat{L} & 0 & 0 \\
0 & 0 & 0 & 0 & \hat{L} & 0 \\
0 & 0 & 0 & 0 & 0 & \hat{N}
\end{bmatrix}
+
\begin{bmatrix}
\delta C_{11} & \delta C_{12} & \delta C_{13} & \delta C_{14} & \delta C_{15} & \delta C_{16} \\
\delta C_{12} & \delta C_{22} & \delta C_{23} & \delta C_{24} & \delta C_{25} & \delta C_{26} \\
\delta C_{13} & \delta C_{23} & \delta C_{33} & \delta C_{34} & \delta C_{35} & \delta C_{36} \\
\delta C_{14} & \delta C_{24} & \delta C_{34} & \delta C_{44} & \delta C_{45} & \delta C_{46} \\
\delta C_{15} & \delta C_{25} & \delta C_{35} & \delta C_{45} & \delta C_{55} & \delta C_{56} \\
\delta C_{16} & \delta C_{26} & \delta C_{36} & \delta C_{46} & \delta C_{56} & \delta C_{66}
\end{bmatrix}
\tag{4}
$$

where $\hat{A} = 3(C_{11}+C_{22})/8 + C_{12}/4 + C_{66}/2$, $\hat{C} = C_{33}$, $\hat{N} = (C_{11}+C_{22})/8 - C_{12}/4 + C_{66}/2$,

$\hat{L} = (C_{44}+C_{55})/2$, and $\hat{F} = (C_{13}+C_{23})/2$. The carat over the symbols indicates that the

moduli are azimuthal averages, and can be thought of as the apparent radially anisotropic

moduli that would be observed in the observational coordinates. Apparent azimuthally

averaged seismic velocities can be defined similarly

$$(\hat{V}_{sh} = (\hat{N}/\rho)^{1/2}, \hat{V}_{sv} = (\hat{L}/\rho)^{1/2}, \hat{V}_{ph} = (\hat{A}/\rho)^{1/2}, \hat{V}_{sv} = (\hat{C}/\rho)^{1/2}).$$

As discussed in the Introduction, it is important to distinguish between the coordinates used to

describe the medium's properties and the coordinates in which the observations are made. We

define anisotropy in the coordinate system of the medium in which the 3-axis is parallel to the

medium's symmetry axis and the 1- and 2-axes lie in the foliation plane as shown in **Figure 1**. In

these coordinates, the five Love moduli completely describe the anisotropy, and because the

medium is hexagonally symmetric there is no (inherent) azimuthal anisotropy. Following *Xie et*

al. [2015], we refer to anisotropy in the coordinate frame of the medium as "inherent". To

describe the anisotropy fully, we include the medium's orientation by specifying the dip and

strike angles. Thomsen (1986) defined useful summaries of inherent anisotropy:

1
2
3
4
5
6
7
8
9
10
11
12
13
14
15
16
17
18
19
20
21
22
23
24
25
26
27
28
29
30
31
32
33
34
35
36
37
38
39
40
41
42
43
44
45
46
47
48
49
50
51
52
53
54
55
56
57
58
59
60

$$\gamma \equiv \frac{N-L}{2L} \qquad \varepsilon \equiv \frac{A-C}{2C} \qquad \delta \approx \frac{F+2L-C}{C} \tag{5}$$

where, in particular, we refer to γ as "inherent S-wave anisotropy". In contrast, in the observational coordinates the description of anisotropy is "apparent". The azimuthally averaged elastic tensor, given by the first matrix on the right-hand-side of equation (4), summarizes the apparent radial anisotropy of the medium, which depends both on the inherent moduli and the dip angle. As defined by *Xie et al.* [2015], a useful summary is the apparent S-wave radial anisotropy:

$$\hat{\gamma} \equiv \frac{\left(\hat{N}-\hat{L}\right)}{2\hat{L}}, \tag{6}$$

where, as in equation (4), the carat over a symbol indicates that the quantity is apparent. Apparent S-wave radial anisotropy is what most studies refer to simply as "radial anisotropy" [e.g., *Shapiro et al.,* 2004; *Xie et al.,* 2015]. Although there is no inherent azimuthal anisotropy in our model, apparent Rayleigh (or SV) wave azimuthal anisotropy emerges in the observational frame by tilting the medium, which we represent with dimensionless amplitude:

$$\hat{\Gamma} \equiv \frac{\left((C_{55}-C_{44})^2+(C_{45})^2\right)^{1/2}}{2\hat{L}} \tag{7}$$

and direction $\hat{\varphi}_{FA} = \frac{1}{2}\tan^{-1}(C_{45}/(C_{55}-C_{44}))$. $\hat{\Gamma}$ is equivalent to $|G|/2L$ used in other studies [e.g., *Yao et al.*, 2010; *Lin et al.*, 2011; *Yuan et al.*, 2011; *Xie et al.,* 2015].

Thus, the anisotropy of a THS medium can be described completely in terms of the inherent Love moduli and the dip angle. Alternately, it can be described partially by the apparent radial and azimuthal anisotropy, which depend on the inherent anisotropy and tilt. In particular, for the

same inherent elastic tensor, the nature of the apparent anisotropy will depend on the orientation of the medium. **Figure 6** demonstrates qualitatively how apparent SV-wave (or Rayleigh wave) azimuthal anisotropy, $\hat{\Gamma}$, and apparent S-wave radial anisotropy, $\hat{\gamma}$, will vary as a function of the dip angle of the symmetry axis. These curves are computed from a simple elastic tensor with a slow vertical symmetry axis with inherent S-wave anisotropy γ normalized to unity. For this model, the amplitude of apparent azimuthal anisotropy $\hat{\Gamma}$ increases monotonically with increasing dip angle θ, and the apparent radial anisotropy $\hat{\gamma}$ decreases with increasing dip. When the foliation plane is flat or equivalently the symmetry axis is vertical (dip θ=0°), there is strong positive apparent S-wave radial anisotropy but no azimuthal anisotropy. As the dip angle increases, the apparent radial anisotropy becomes negative and azimuthal anisotropy attains its maximum value.

Observations of strong positive apparent radial anisotropy but low amplitude apparent azimuthal anisotropy are consistent with a subhorizontal foliation plane and a slow nearly vertical symmetry axis (i.e., a VHS medium). In contrast, observations of a strongly negative apparent radial anisotropy and strong azimuthal anisotropy are consistent with a subhorizontal symmetry axis (i.e., a HHS medium). Simultaneous observations of intermediate values of radial and azimuthal anisotropy are consistent with a tilted symmetry axis (i.e., a THS medium). Therefore, technically, with surface wave observations, we can invert for a description of the THS medium. However, because surface waves are strongly sensitive only to some of the seven depth-depdendent variables that describe the THS medium, a straightforward inversion is impractical with surface wave data alone. Following *Xie et al.* [2015], we employ a Bayesian Monte Carlo inversion method to estimate distributions of THS media that agree with the data. Such posterior distributions reflect both variances within and covariances between all model variables. Here, we

present models in terms of inherent anisotropy and the dip and strike angles, but because most studies present apparent radial anisotropy and apparent azimuthal anisotropy we also convert our results into these quantities to aid comparison with other studies (section 6.1).

4. Model Specification: Parameterization and Constraints

Figure 7 schematically represents the model parameterization, which is similar in many respects to the parameterization applied by *Xie et al.* [2015]. Like *Xie et al.* [2015] we parameterize the crust in terms of a depth-varying THS medium that is described by seven inherent parameters (A, C, N, L, F, strike ϕ and dip θ) (**Fig. 1**). The depth dependences of the elastic moduli A, C, N, L, and F are represented by five B-splines in the crystalline crust from the base of the sediments to Moho. For *Xie et al.* [2015], at each location, the dip and strike angles (tilt angles θ, ϕ) that define the orientation of the symmetry axis of anisotropy are constant through the crystalline crust. Here, however, we introduce a discontinuity in the crust that allows the dip angle to jump smoothly from values above and below a mid-crustal dip boundary set at one third of the crystalline crustal thickness at each location. The strike angle, however, remains constant throughout the crust. Like *Xie et al.* [2015] we assume the sediments to be isotropic. We constrain crustal anisotropy to have a slow symmetry axis consistent with studies of crustal petrology as discussed in section 6.2.2. In addition, the introduction of a fast symmetry axis tends to be incompatible with the frequency dependence of our observations.

We introduce the mid-crustal discontinuity in dip angle because we find that we are unable to fit our observations over large areas, particularly in Tibet, without it. **Figure 5** illustrates this point. The difference between Love and Rayleigh wave phase speeds at Point A in Tibet (**Fig. 5a**) cannot be fit with a model in which the dip angle is constant in the crust (black line), but can be

fit when we allow dip angle to change once discontinuously in the crust (red line). We choose the value of one third of the crustal thickness as the location of the discontinuity in accordance with the study of *Deng et al*. [2015], who observed a discontinuity at about this depth in northern Tibet based on joint inversion of surface wave dispersion and receiver function data. In contrast, in some areas the data can be fit by the model with a constant crustal dip, such as Points B and C in the Qilian and Chuandian terranes (**Fig. 5b,g**). At Point D in the Yunnan-Guizhou plateau (**Fig. 5j**), two crustal dip angles are needed to fit the data but the misfit produced by the single dip model is not as large as within Tibet.

We use the China reference model produced by Shen et al. [2016] as the crustal reference around which perturbations are applied in the inversion. This is an isotropic model based on Rayleigh wave data, which most strongly constrain the elastic modulus L (related to V_{SV} in a TI medium). We use the model to define a reference for the four elastic moduli and density: $A_0(r)$, $C_0(r)$, $N_0(r)$, $L_0(r)$, and $\rho_0(r)$, where r is the radius within the Earth. Also, we use it to define sedimentary structure (seismic velocities and density increase linearly with depth and thickness), Moho depth, and Q(r), which we do not change in the inversion.

Based on data sensitivity (e.g., **Fig. 4c,d**), we apply several prior constraints to the seven depth-dependent parameters that describe the oriented elastic tensor. We apply weaker constraints on parameters that are highly data sensitive, and stronger constraints on parameters to which the data have little sensitivity. Therefore, the shear moduli L and N are relatively weakly constrained, and are perturbed within the range of $L_0(1\pm0.3)$. In contrast, the compressional moduli are strongly constrained, and we set $C = (1.77)^2 L \approx 3.13N$ where 1.77 is the Vp/Vs ratio, and similarly we set $A=(1.77)^2 N$. Thus, the inherent P-wave anisotropy $\varepsilon = (A-C)/2C$ equals inherent S-wave anisotropy $\gamma = (N-L)/2L$. The modulus $\eta = F/(A-2L)$ is freely perturbed within

[0.8,1.1]. This is a narrower range for η than used by *Xie et al.* [2015] (in that work η ∈ [0.6,1.1])

in order to eliminate the in strike angle. *Xie et al.* [2015] found that two groups of models with

orthogonal strike directions fit the data equally well, and these two groups of models have

similar inherent S-wave anisotropy and dip but different values of η. Therefore, reducing the

range of η eliminates this bifurcation and simplifies the resulting models. We discuss the impact

of this constraint on the strike angle in section 5.2. The dip angle θ and strike angle ϕ range

between 0° and 90°.

Because Love wave sensitivity is shallower than Rayleigh wave sensitivity (**Fig. 4c,d**) at a given

period, the amplitude of inherent S-wave anisotropy γ is poorly determined in the Tibetan

lowermost crust. This is illustrated in **Figure 8**, which shows the results of three inversions of the

same data in Tibet (Point A) but with different constraints on γ: (a) γ ≥ 0 throughout the crust,

(b) γ > 0 throughout the crust but γ = 0 at the base of the crust, and (c) 0 ≤ γ ≤ 10% throughout

the crust. These constraints produce very different estimates of γ below 50 km depth in the crust.

In particular, without a constraint beyond the positivity constraint (γ ≥ 0), the estimate of γ in the

lowermost crust of Tibet becomes unstable. For this reason, we seek a small amplitude model

here and apply the constraint that 0 ≤ γ ≤ 10% throughout the crust across the entire study

region. The result of this constraint is that γ will tend to be approximately constant with depth in

the lowermost crust of Tibet.

It is with some trepidation that we have modeled the sediments as isotropic because Tibet is

surrounded by large basins where there is strong evidence of anisotropy. However, because the

model of *Shen et al. [2016]* is based exclusively on Rayleigh wave data it does not provide a

particularly accurate reference for sedimentary structure, in particular sedimentary thickness.

Thus, inferences we might draw here about sedimentary anisotropy would be suspect. In order to

constrain the structure of the sediments better, additional data such as receiver functions or the

H/V ratio, which are more sensitive to the shallower depths, should be added. We discuss

sedimentary anisotropy in section 6.2.3 where we provide evidence that the sediments are

strongly anisotropic, so much so that we are forced to eliminate the amplitude constraint on γ in

the sediments. However, modeling them as isotropic does not affect our primary conclusions,

although it does mean that we are not able to fit our data well within the basins.

In terms of the mantle parameterization, it is not clear if hexagonal symmetry with a slow

symmetry axis is physically appropriate to represent mantle anisotropy. If mantle anisotropy is

produced by the lattice-preferred orientation (LPO) of olivine, then the mantle could be modeled

either as hexagonally symmetric with a fast symmetry axis or as orthorhombic, depending on

whether the two slower olivine crystal axes scatter randomly or not [*Christensen*, 1984]. In

contrast, if the mantle anisotropy is caused by partial melt, then mantle anisotropy could be

modeled either as hexagonally symmetric with a slow symmetry axis or orthorhombic,

depending on the shape of the melt pockets [e.g., *Thomsen and Anderson*, 2015]. In any case,

because our surface wave observations extend only up to 50 sec period they poorly constrain

mantle anisotropy beneath Tibet. Tests of several different mantle parameterizations and

constraints show, however, that changes in the parameterization affect estimated crustal

structures within the estimated uncertainties.

For these reasons, we parameterize mantle anisotropy (**Fig. 7**) simply in terms of apparent

quantities rather than inherent properties, and beneath 200 km the model is set to be AK135

[*Kennett et al.*, 1995], which is isotropic. In particular, we describe the mantle as a VHS medium

plus additional apparent azimuthal anisotropy. In this case, mantle radial anisotropy decouples

from azimuthal anisotropy and both are the apparent quantities. We estimate $\hat{V}_{sv}$ as a free

parameter in the uppermost mantle, represent it with five B-splines, and allow it to vary within

the range $\hat{V}_{sv0}(1 \pm 0.15)$, where the reference value $\hat{V}_{sv0}$ is from *Shen et al.* [2016]. We compute

$\hat{V}_{sh}$ from $\hat{V}_{sv}$ by assuming a constant value of $\hat{\gamma} = 4.5\%$, a value that is consistent with the average

of mantle apparent radial anisotropy across the study region determined by *Shapiro et al.* [2004].

This is presented in **Figure 7** as $\hat{V}_{SH} = f(\hat{V}_{SV})$, which should be read " $\hat{V}_{SH}$ is a function of $\hat{V}_{SV}$ ".

We also estimate the apparent amplitude of azimuthal anisotropy $\hat{\Gamma}$ (eqn. (7)) and the local fast

direction $\hat{\varphi}$, both of which are set to be constant with depth in the mantle. We further set

$\hat{V}_{PV} = 1.77\hat{V}_{SV}$ and $\hat{V}_{PH} = 1.77\hat{V}_{SH}$, which sets apparent P-wave anisotropy equal to apparent S-

wave anisotropy. $\hat{\eta}$ is freely varying within the range [0.8,1.1]. Because we do not infer any

inherent properties of the mantle anisotropy we do not show mantle anisotropy in plots of

inherent anisotropy. However, plots of apparent anisotropy do include mantle anisotropy. In any

event, we will focus our discussion on the crustal part of the model.

5. Results

The Bayesian Monte Carlo inversion is based on the observed data (described in section 2), a

forward computation algorithm (described by *Xie et al.* [2015] in detail), a starting model, and

prior information consisting of constraints on the model. As discussed in section 4, the starting

model comes from *Shen et. al. [2016],* which is an isotropic Vsv model derived exclusively from

Rayleigh waves, and the constraints guide the formation of the prior distribution at each location.

The Bayesian Monte Carlo inversion method is very similar to that described in a series of recent

papers by *Shen et al.* [2013a,b] and elsewhere [e.g., *Shapiro and Ritzwoller*, 2002; *Zheng et al.*,

2011; *Yang et al.*, 2012; *Zhou et al.*, 2012; *Shen et al.*, 2013c; *Tian et al.*, 2013; *Xie et al.*, 2013;

Deng et al., 2015; *Kang et al.*, 2015*; Shen et al.*, 2015; *Shen and Ritzwoller*, 2016]. Here, we invert the data at every location on a 0.5° x 0.5° grid and produce a set of models that define the posterior distribution of models that fit the data acceptably. We summarize each posterior distribution by its mean, which we refer to as the "mean model", and standard deviation, which together define the final model with an estimate of uncertainty at each depth and for each model variable. We present the model here in terms of the inherent elastic tensor and its orientation (dip and strike). A discussion of the apparent anisotropy that results from this representation occurs in section 6.1. Examples of marginal posterior distributions of selected model characteristics are presented in **Figures 9** and **10** for 10 km and 30 km depth, respectively, and are discussed further below.

5.1 Example results at four locations

We first present the results of the inversion of the data presented in **Figure 5** at the four locations identified in **Figure 2a**: Point A in eastern Tibet, Point B in the Qilian terrane north of Tibet, Point C in the central Chuandian terrane just off southeastern edge of the Tibetan plateau, and Point D in the Yunnan-Guizhou plateau.

At Point A, the Love-Rayleigh phase velocity difference increases with period, while the amplitude of Rayleigh wave azimuthal anisotropy decreases with period (**Figure 5a-c**). **Figure 5a-c** shows that the data are fit well (red lines) by the mean model with the parameterization that allows two different dip angles in the crust. The fit delivered by the mean models produced from inversions with two other parameterizations are also shown in **Figure 5a-c**: an isotropic model (green lines) and a model with a constant dip angle throughout the crust (black lines). Neither of these models can fit the Love wave and Rayleigh wave phase speeds simultaneously across most

of Tibet. This provides the primary justification for the introduction of the discontinuity in dip

angle in the middle crust in our parameterization.

Aspects of the posterior distributions at Point A are presented in **Figures 9** and **10**, which display

marginal distributions for inherent $\sqrt{L/\rho}$, $\sqrt{N/\rho}$, η, dip angle θ, and strike angle ϕ at depths

of 10 km and 30 km. These are five of the seven parameters that describe the elastic tensor and

its orientation at each depth. The other two (compressional moduli A, C) are scaled from the

shear moduli L and N and are, therefore, not shown. At both depths L and N are well

constrained; the standard deviations of the posterior distributions are less than about 1% at both

10 km and 30 km depth. The strike angle is constant in the crust and is also well constrained,

with a standard deviation of about 3°. In contrast, η is not well constrained at either depth, which

tends to be true across the study region. The most notable difference between the two depths is

the very different dip angle at 10 km (71°±9°) compared with 30 km (8°±5°). The foliation plane

dips steeply in the upper crust and is sub-horizontal in the lower crust at this location in eastern

Tibet, and across most of Tibet, as we will show. In the lower crust here, the foliation plane is

observationally indistinguishable from horizontal (i.e., the symmetry axis is indistinguishable

from vertical).

This information can be viewed in a different way in **Figure 11** in which one standard deviation

bounds around the mean of the posterior distribution are presented as a function of depth for the

dip angle and inherent S wave anisotropy, γ (eqn. (5)). The change in the dip angle with crustal

depth is shown for Point A in Tibet in **Figure 11a** and γ is seen in **Figure 11b** to range from 3-

5% in the uppermost crust (depth < 10 km), to about 7% at 40 km depth, and then decrease with

depth to ~4-5% in the lowermost crust.

At Point B, which is located in the Qilian terrane just north of Tibet, the isotropic model also does not fit the data (**Fig. 5d-f**), thus crustal anisotropy is also required outside of Tibet. However, the data can be fit with either model in which we allow the dip angle to change in the middle crust or constrain it to be constant throughout the crust. The reason for this is seen in **Figure 11c**, which shows that the dip angle is essentially indistinguishable between the upper and lower crust at this location (~40°). **Figure 11d** shows that γ is approximately constant with depth, averaging about 4% across the crust at this location.

At Point C, the data differ from those at both Points A and B in that the Love-Rayleigh phase speed difference can nearly be fit with an isotropic model (**Fig. 5g**; indicating near-zero apparent radial anisotropy). However, the high amplitude of azimuthal anisotropy guarantees the existence of crustal anisotropy. Similar to Point B, the dip angle (~60°) at Point C does not change strongly with depth across the crust (**Fig. 11e**), but the dip angle is steeper than at Point B. The amplitude of inherent S-wave anisotropy γ averages between 2% and 3% across most of the crust (**Fig. 11f**), which is weaker than at Points A and B.

Crustal anisotropy at Point D is more similar to Tibet in that two dip angles are needed to fit the data shown in **Figure 5j-l**. Although the dip angle (**Fig. 11g**) in the upper crust is similar to that in Tibet (>70°), the dip angle in the lower crust is larger (~20°) and is distinguishable from zero. Thus, the lower crustal foliation plane in the Yunnan-Guizhou plateau is not as horizontal as beneath Tibet, but is shallowly dipping. Also, the vertical distribution of inherent S-wave anisotropy at Point D (**Fig. 11h**) differs from Tibet. The anisotropy in Tibet is strong throughout the crust, whereas beneath the Yunnan-Guizhou plateau it is concentrated in the uppermost (~4%) and lowermost crust (~5%) with a minimum at a depth of about 15 km (~1.5%).

In section 6.1, we discuss the apparent crustal anisotropy computed from the inherent anisotropy

and dip angle discussed here, as well as apparent mantle anisotropy.

5.2 Results across the entire region: mean of the posterior distribution

Aspects of the resulting model (dip angle θ, inherent S wave anisotropy γ), defined as the mean

of the posterior distribution at each depth, are shown in **Figure 12** at depths of 10 km and 30 km

in the crust. These depths bracket the discontinuity in dip angle across the entire study region.

The estimated strike of anisotropy, which is constant with depth within the crust, is shown in

Figure 13a in which the orientation of the bars indicates the strike orientation (ϕ). As described

in Section 4, we have deliberately narrowed the allowed range of η by eliminating small η

values; thus our resulting models approximately possess so-called elliptical anisotropy [e.g.,

Thomsen, 1986; *Xie et al.*, 2015]. As a consequence, the crustal strike orientation generally

follows the Rayleigh wave fast axis orientation at short periods (**Fig. 3c**). However, as discussed

by Xie et al. [2015], if η is allowed to vary broadly enough there will be two subsets of models in

the posterior distribution with orthogonal strike angles. We circumvented this bifurcation by

constraining the η to be relatively large. Nevertheless, at each location there is another strike

orientation that is consistent with our data, which we show in **Figure 13b**. We note that if the dip

angle is small so that the foliation plane is nearly horizontal, the strike angle loses its

significance.

At 10 km depth (**Fig. 12a,b**), the foliation plane in the upper crust is steeply dipping across most

of the study region, including the Tibetan plateau and its surroundings. In contrast, the Qaidam

basin, Ordos block, southern Tibet, and the Sichuan basin are characterized by shallow dip

angles in the shallow crust. The inherent S-wave anisotropy (**Fig. 12b**) ranges from ~2% to ~6%

across most of the study region. Inherent S-wave anisotropy in the shallow crust is not noticeably stronger in Tibet than in its surrounding areas. Because the sediments in the model are isotropic, anisotropy in the sediments may bias γ to larger values at 10 km depth beneath the deep sediments of the Sichuan and Qaidam basins.

At 30 km depth (**Fig. 12c,d**), the interior of eastern Tibet has a sub-horizontal foliation plane that is largely indistinguishable from a VHS medium. Near the boundaries of the Tibetan plateau, particularly between Tibet and the western Yangtze craton (including the Sichuan Basin) and in the Qilian terrane north of Tibet, the medium is moderately to steeply dipping in the middle to lower crust (**Fig. 12c**). The inherent S-wave anisotropy (**Fig. 12d**) is relatively large across the entire region of study with amplitudes ranging from about 3% to 6%. The strongest inherent S-wave radial anisotropy is observed in the interior of eastern Tibet and the Yunnan-Guizhou plateau south of the Sichuan basin. Weaker inherent S-wave anisotropy is observed near the eastern boundary of the Tibetan plateau and in the Sichuan basin and Ordos block. At most places, γ grows with depth in the crust but not beneath the major basins.

For a more complete view of crustal anisotropy, two vertical profiles of crustal inherent S-wave anisotropy and dip angle are presented in **Figure 14**. The locations of the two profiles are shown in **Figure 2b**. Profile A starts just north of the Kunlun fault east of the Qaidam basin, runs through the Songpan-Ganzi terrane of eastern Tibet and the Chuandian terrane, off the southeastern margin of Tibet, and into the Yunnan-Guizhou plateau. Profile B runs from the boundary between the Lhasa and Qiantang terranes in eastern Tibet, through the Qiangtang and Songpan-Ganzi terranes, and northeast off the Tibetan plateau to terminate just within the Ordos block. **Figures 14a** and **14b** present the dip angles along these profiles in two ways: color-coded and also with orientation bars that lie along the foliation plane at 50 km lateral intervals. The

1
2
3
4
5
6
7
8
9
10
11
12
13
14
15
16
17
18
19
20
21
22
23
24
25
26
27
28
29
30
31
32
33
34
35
36
37
38
39
40
41
42
43
44
45
46
47
48
49
50
51
52
53
54
55
56
57
58
59
60

vertical bifurcation of the dip angle between the steeply dipping upper and shallowly dipping lower crust is the most striking feature of both profiles. The principal exception occurs near the southeastern border of Tibet where steeping dipping anisotropy appears throughout the entire crust (**Fig. 14a**). **Figures 14c** and **14d** present inherent S-wave anisotropy (γ) and illustrates that along these profiles γ tends to grow with depth in the crust. In general γ is more homogeneous laterally than vertically, although it is smaller beneath the Ordos block than elsewhere along these profiles. As discussed earlier, γ is poorly estimated below 50 km depth.

Because the lower crustal dip angle is small across most of the study region, the strike angle for the lower crust has little significance. This may be one of the reasons why a single strike angle at each location across crust suffices to fit the data in Tibet. As discussed in section 6.1, this is related to the fact that there is very low amplitude apparent azimuthal anisotropy in the lower crust of Tibet.

Discussion of the interpretation of these results is delayed until section 6.2. Comparison with apparent radial and azimuthal anisotropy, which are the more commonly estimated quantities in surface wave studies, is found in section 6.1. We also show γ at 5 km above Moho in section 6.3.1 while discussing the vertical distribution of the amplitude of inherent anisotropy.

5.3 Data misfit

The misfit to the data (Rayleigh wave phase speeds, Love wave phase speeds, amplitude and fast axis directions of Rayleigh wave azimuthal anisotropy) is presented as the square root of the reduced chi-squared misfit in **Figure 15**. Specifically, misfit is defined as follows. For model m, let S(m) be the reduced chi-square:

$$S(m) = \frac{1}{N} \sum_{i=1}^{N} \frac{(D(m)_i - D_i)^2}{\sigma_i^2}$$

(8)

where D_i is the observation of datum i, $D(m)_i$ is that datum predicted from model m, σ_i is the

standard deviation of datum i, and N is the total number of observations. The error bars in

Figure 5 illustrate the nature and number of the observations and their standard deviations. The

misfit presented in **Figure 15** is the square root of $S(m)$ across the study region. A value of unity

would indicate that the data are fit on average at the level of one standard deviation. The data

across most of the region are fit at a level better than 1.5 standard deviations, with the exception

of the large sedimentary basins (Sichuan, Qaidam). To fit the data in the basins we would need to

introduce anisotropy to the sediments, which complicates the inversion and is beyond the scope

of this paper.

5.4 Results across the entire region: standard deviation of the posterior distribution

As discussed by *Shen and Ritzwoller* [2016], it is not entirely straightforward how to use the

posterior distribution to quantify model uncertainty. They argue that the standard deviation of the

posterior distribution does not provide an estimate of the effect of systematic errors and provides

an over-estimate of the effect of non-systematic errors. They go on to quantify non-systematic

errors in several different ways and estimate that the standard deviation of the posterior

distribution over-estimates the effect of non-systematic errors by about a factor of 4. Here, we

present the standard deviation of the posterior distribution to guide the use of the model and refer

to it as model uncertainty, but it should be understood that this uncertainty does not include

potential systematic contributions and is probably a very conservative estimate of non-systematic

error.

The standard deviation of the posterior distribution (uncertainty) is shown in **Figure 1**6 at depths of 10 and 30 km for dip angle and inherent S-wave anisotropy γ. The uncertainty for dip lies between 5° and 15° at both 10 and 30 km depths in most regions remote to the Sichuan and Qaidam basins (**Figures 16a,b**). (The uncertainty beneath the basins is magnified because the data cannot be fit as well there due to the fact that we have not included anisotropy in the sediments.) In contrast, as shown in **Figure 16e**, the standard deviation of the posterior distribution for the strike angle is smaller, averaging about 7° outside the basins, but is larger near the periphery of our study region where the fast axis directions of Rayleigh waves are less well constrained. One reason the strike uncertainty is smaller than the dip uncertainty is because the strike angle is constrained to be constant within the crust, whereas the dip angle is allowed to change within the crust. A second reason is that strike is constrained in a direct way by observations of the Rayleigh wave fast azimuth, whereas the dip angle trades off with the inherent elastic moduli and together they are less directly constrained by our observations. The average value of 7° is close to the uncertainty for Rayleigh wave fast azimuth at short periods (e.g., **Figures 5c,f,i,l**).

The average uncertainty for inherent S-wave anisotropy (γ) is about 1.2% at 10 km depth and slightly larger at 30 km depth (**Figures 16c,d**). At both depths, the uncertainty is larger outside of Tibet. At 30 km depth, the uncertainty is extremely large in the southeastern part of the study region. This is because uncertainty grows near to the Moho due to trade-offs across the interface. The Moho lies between 35 and 40 km where large uncertainties exist in γ. The estimated uncertainty in γ at 5 km above Moho is shown and discussed in section 6.3.1. Formally, it is larger at this depth than shallower in the crust but the result we show later actually underestimates uncertainty below 50 km depth because it reflects the weak anisotropy constraint

($\gamma \leqslant 10\%$), which stabilizes the inversion below a depth of 50 km and reduces the uncertainty estimate.

6. Discussion

6.1 Model presented in terms of apparent anisotropy

In section 5, we present the estimated THS model in terms of the mean of the posterior distribution of the inherent elastic moduli and orientation at each depth. Particular emphasis is placed on the inherent S-wave anisotropy γ (eqn. (5)) and the dip and strike angles (θ,ϕ) that describe the orientation of the medium because these are the variables that are best constrained by surface wave data. The inherent representation of anisotropy presents the elastic tensor in the coordinate frame of the medium as shown in **Figure 1**. In the medium frame, the 3-axis of the coordinate system aligns with the symmetry axis of the medium and there is no azimuthal anisotropy. However, in the coordinate system of observation the 3-axis lies normal to the Earth's surface and observations of anisotropy depend on how components of the elastic tensor are affected by the tilt of the medium. When a hexagonally symmetric medium is tilted, both apparent S-wave radial anisotropy ($\hat{\gamma}$, eqn. (6)) and apparent SV-wave azimuthal anisotropy ($\hat{\Gamma}$, eqn. (7)) may be observed. Indeed, most studies of anisotropy using surface waves have described anisotropy in terms of $\hat{\gamma}$ [e.g., *Shapiro et al.*, 2004; *Panning and Romanowicz*, 2006; *Marone et al.*, 2007; *Nettles and Dziewoński*, 2008; *Duret et al.*, 2010; *Huang et al.*, 2010; *Moschetti et al.*, 2010; *Yuan et al.*, 2011; *Xie et al.*, 2013; *French and Romanowicz*, 2014] or $\hat{\Gamma}$ [e.g., *Simons et al.*, 2002; *Marone and Romanowicz*, 2007; *Yao et al.*, 2010; *Lin et al.*, 2011; *Yuan et al.*, 2011; *Pandey et al.*, 2015]. As discussed by *Xie et al.* [2015] the apparent values can be computed from the inherent values. In order to aid comparison with other studies, we

summarize here the apparent S-wave radial anisotropy and apparent azimuthal anisotropy computed from the estimated inherent elastic tensor and its orientation.

Figure 17 presents results for crustal apparent radial anisotropy $\hat{\gamma}$ and apparent azimuthal $\hat{\Gamma}$ anisotropy at the same locations shown for inherent S-wave anisotropy γ and dip angle θ in **Figure 11**. **Figure 17** also presents results for $\hat{\gamma}$ and $\hat{\Gamma}$ in the mantle because we parameterize the mantle in terms of apparent quantities. Mantle apparent radial anisotropy $\hat{\gamma}$ is set to 4.5% at all locations, although $\hat{V}_{SV}$ and apparent azimuthal anisotropy $\hat{\Gamma}$ change spatially.

Apparent radial anisotropy is qualitatively similar in the crust at Points A and D (**Fig. 17a,g**), being weakly negative in the upper crust and more strongly positive in the lower crust. $\hat{\gamma}$ attains a maximum value of about 7% at about 45 km depth at Point A and is negative (-1.5%) in the upper crust. Because the foliation plane of the lower crust is sub-horizontal across most of Tibet, inherent S-wave anisotropy γ and apparent radial anisotropy $\hat{\gamma}$ in the lower crust are very similar at Point A (**Figs. 11b, 17a**). Also at Points A and D, apparent azimuthal anisotropy $\hat{\Gamma}$ dominantly arises from the upper crust. Apparent azimuthal anisotropy is indistinguishable from zero in Tibetan lower crust (**Fig. 17b**), thus the lower crustal strike angle has little significance.

At Points B and C, $\hat{\gamma}$ is approximately constant in the crust. At Point C it is indistinguishable from zero even although the inherent anisotropy γ averages about 3%. This is caused by a dip angle of about 60° across the entire crust, a value that lies near the zero-crossing of anisotropy shown in **Figure 6**. $\hat{\Gamma}$ also is approximately constant with depth in the crust at Points B and C.

Mantle apparent radial anisotropy (4.5%) tends to be stronger than crustal radial anisotropy except at Point A in Tibet where lower crustal $\hat{\gamma}$ reaches 7%. At Point A in Tibet, upper crustal

apparent azimuthal anisotropy (2-3%) is stronger than mantle apparent azimuthal anisotropy

(~1.2%).

Horizontal slices at depths of 10 km and 30 km are presented for the apparent quantities $\hat{\gamma}$ and

$\hat{\Gamma}$ in **Figure 18**, to contrast with the inherent quantities γ and θ found in **Figure 12**. Negative $\hat{\gamma}$

commonly coincides with large $\hat{\Gamma}$ in the shallow crust, again due to large dip angle and is

explained by **Figure 6**. Similarly, in the deep crust large $\hat{\gamma}$ coincides with small $\hat{\Gamma}$ due to a

shallow dip angle. Finally, vertical transects of the apparent quantities $\hat{\gamma}$ and $\hat{\Gamma}$ are presented in

Figure 19 for comparison with the inherent quantities plotted in **Figure 14**.

Compared with inherent S-wave anisotropy γ, the apparent radial anisotropy $\hat{\gamma}$ (**Fig. 18a,c;**

19a,b) displays much stronger lateral variations because it reflects variations in dip angle in

addition to inherent anisotropy. The steep dip angle in the upper crust (**Fig. 12a**) produces

negative apparent radial anisotropy (apparent V_{SH} < apparent V_{SV}) across much of the study

region (e.g., **Fig. 18a**), with the principal exceptions occurring beneath large sedimentary basins.

Figure 19 shows that the negative apparent anisotropy in the upper crust extends beneath much

of both vertical profiles. Such negative $\hat{\gamma}$ values was observed across parts of Tibet by *Xie et al.*

[2013], who interpreted them as evidence for steeply dipping fractures or faults in the shallow

Tibetan crust. Due to the shallow lower crustal dip angles across much of the study region, γ and

$\hat{\gamma}$ are similar in the lower crust. Thus across much of the region, **Figure 12c** is similar to **Figure**

18c, with the notable exceptions being in regions with steep lower crustal dip angles such as the

regions flanking Tibet. Profile A in **Figure 19a** illustrates one of these exceptions (longitudes

between 101.3° and 102.5°) and shows that negative apparent radial anisotropy extends

throughout the crust in the central-to-southern part of the Chuandian terrane near the southeast

border of Tibet.

Azimuthal anisotropy is not an inherent property of the elastic tensor, but reflects the directional dependence of Rayleigh wave speeds that results from the amplitude of inherent anisotropy and the tilting of the medium. When the dip angle is small, as it is across much of the lower crust of Tibet (**Fig. 12c**), the apparent azimuthal anisotropy is minimal (**Fig. 18d**). In contrast, lower crustal apparent azimuthal anisotropy (**Fig. 18a**) is particularly strong near the periphery of Tibet where the lower crustal dip angle is steep. Unlike the lower crust, the upper crust is steeply dipping across much of the study region, so upper crustal apparent azimuthal anisotropy is also strong across most of the region (**Fig. 18b**). Apparent azimuthal anisotropy, being strong in the upper crust and weak in the lower crust at most locations, is seen clearly in the two vertical profiles in **Figure 19c,d**.

In summary, apparent azimuthal $\hat{\Gamma}$ and radial $\hat{\gamma}$ anisotropy bifurcate vertically in most of the study region. Apparent azimuthal anisotropy is strong principally in the upper crust whereas apparent radial anisotropy is strong mostly in the lower crust. The principal exception to this bifurcation lies predominantly near the periphery of Tibet, where the dip angle is nearly constant throughout the crust.

6.2 Geological and physical significance

6.2.1 Regionalization

The results presented here illustrate that the inferred crustal anisotropy is of two principal types that segregate into the two regions depicted in **Figure 20**: Region 1 (red color, Tibet and the Yunnan-Guizhou plateau region) and Region 2 (blue color, regions near the periphery of Tibet).

The sedimentary basins define a third region that we do not discuss here.

Region 1: In the interior of eastern Tibet, the upper crust has a steeply dipping foliation plane, which generates negative apparent radial anisotropy, and the middle-to-lower crust has a sub-horizontal foliation in which the dip angle θ is often indistinguishable from zero. This results in a large positive apparent Vs radial anisotropy in the lower crust. Tibet itself has high seismicity with earthquakes occurring to a depth of about 15-20 km within Tibet [*Chu et al.*, 2009; *Zhang et al.*, 2010; *Sloan et al.*, 2011]. Therefore, the upper crust to this depth probably undergoes brittle deformation. Steeply dipping foliation could result from fractures or faults that are sub-vertical or steeply dipping. In contrast, the nearly horizontal foliation plane of the middle-to-lower crust may result from the deeper crust undergoing predominantly horizontal ductile deformation in which melt-rich layers or planar mica sheets form in response to the deformation. Interestingly, this pattern of anisotropy is not unique to Tibet, but is also observed south of the Sichuan basin in the Yunnan-Guizhou Plateau.

Region 2: Near the boundary of eastern Tibet and regions north of Tibet, such as the Qilian terrane, there is a depth constant moderate dip angle through the entire crust that results in negative to slightly positive apparent radial anisotropy throughout the crust. From Region 1 to Region 2, the orientation of the middle-to-lower crustal foliation plane rotates from horizontal to moderately or steeply dipping. This lateral change of orientation may result from resistance forces applied by the rigid and relatively undeformed Sichuan basin, Yangtze craton and Ordos block.

6.2.2 Physical significance

Our principal results are represented with a pair of variables at each location and depth from

which we can compute apparent radial and azimuthal anisotropy: inherent S-wave anisotropy γ

and dip angle θ. These variables allow us to predict the primary aspects of our observations.

However, there are many constraints and assumptions underlying these results. Perhaps most

significant amongst these is the assumption that the elastic tensor at all depths in the crust

possesses hexagonal symmetry with a slow symmetry axis.

There are reasons to believe that hexagonal symmetry is a reasonable assumption for the crust.

The cause of crustal anisotropy is related to shape preferred orientation (SPO) and lattice- or

crystal-preferred orientation (CPO) of Earth's materials. In the crust, SPO can be caused by

fluid-filled cracks and layering of materials with different compositions [e.g., *Crampin et al.,*

1984], and both situations can be approximated with a hexagonally symmetric medium with a

slow symmetry axis. Other than SPO, another possible cause of seismic anisotropy is CPO of the

crystallographic axes of elastically anisotropic minerals. Mica and amphibole are primary

candidates for crustal anisotropy [*Mainprice and Nicolas, 1989*]. With increasing mica content, a

deformed rock becomes anisotropic and tends to be approximately hexagonally symmetric with a

slow symmetry axis [*Shao et al., 2016; Weisss et al., 1999*]. *Weiss et al.* [1999] argues that most

deep crustal rocks are quasi-hexagonal, although some studies [e.g., *Tatham et al., 2008*]

conclude that the deep continental crust contains little mica, and amphibole is a more plausible

explanation for deep crustal anisotropy. The presence of amphibole would reduce a rock's

overall symmetry from hexagonal to a lower symmetry such as orthorhombic [*Shao et al., 2016*].

Therefore, in many cases, a hexagonally symmetric medium with a slow symmetry axis is a

reasonable approximation for crustal material, and in this circumstance the inferred dip and strike

angles probably represent the orientation of the foliated anisotropic materials in the crust. But in

the presence of abundant amphiboles, orthorhombic rather than hexagonal symmetry may be

more appropriate. In this case, for example, it would not clear how to interpret the estimated dip angle, which could be understood a proxy for deviation from hexagonal symmetry.

Even when hexagonal symmetry is an appropriate assumption for the anisotropy of crustal rocks, the dip and strikes angles shown in **Figures 12** and **14** represent only one of several possible orientations that are consistent with surface wave data. *Xie et al. [2015]* point out that there are two principal ambiguities in orientation that arise using surface wave data alone to estimate a depth-dependent THS model. First, there is the dip ambiguity that results from a symmetry or a pure geometrical trade-off. Surface waves are not capable of distinguishing between structures with dip angle θ and angle $180° - \theta$ (i.e., left dipping and right dipping). As a result, surface waves cannot distinguish between a structure that dips only toward one-side from a fold that is composed of a combination of left- and right-dipping foliations. Secondly, there is the strike ambiguity. Surface waves do not distinguish between anisotropic structures that differ in strike angle by 90°. This is not a geometrical symmetry but emerges because of covariances between the elastic moduli, and is related to the so-called ellipticity of the elastic tensor, as discussed in *Xie et al.* [2015]. We have eliminated this ambiguity by narrowing the range of η considered but show both strike angles in **Figure 13**. The limitation we imposed on the allowed η values does not affect our principal conclusions. However, it will be important in the future to attempt to distinguish between the two strike angles by invoking other data (e.g., receiver function observations).

6.2.3 Sedimentary basins

As discussed in section 4, we parameterized sedimentary basins as isotropic even though our data present evidence that the sediments are anisotropic, as seen clearly by significant data misfit

under the Sichuan and Qaidam basins in **Figure 15**.

Figure 21 presents a comparison of the results of inversion of our data at a point in the Sichuan

basin (105°, 31°) with (**Fig. 21c,d**) and without (**Fig. 21a,b**) anisotropy in the sediments. Misfit

($S^{1/2}$, equation 8) reduces from 3.44 to 1.40 with the introduction of anisotropy in the sediments

at this point. The inherent anisotropy in the sediments is exceptionally strong (~13%) and the dip

angle is shallow. Thus, the sediments dominantly produce apparent radial anisotropy with little

associated apparent azimuthal anisotropy. Including anisotropy in the sediments does not

strongly change inherent S-wave anisotropy in the crystalline crust (**Fig. 21a,c**) It does, however,

reduce the lower crustal dip angle by about 10°, which more strongly segregates anisotropy

between the upper and lower crust. However, these changes are within the estimated

uncertainties. These results are similar to what we find at other locations within the Sichuan and

Qaidam basins where surface wave observations are reliable and the sediments are thicker than 2

km in the reference model.

We conclude, therefore, that the specification of isotropic sediments changes our estimates of

inherent S-wave anisotropy and dip angle in the crystalline crust within stated uncertainties, and

does not modify the primary conclusions of the study. In the future, parameterizing the sediments

to include anisotropy is recommended, but in doing so it is also advisable to include other

constraints on sedimentary structure such as receiver functions or Rayleigh wave H/V to improve

the estimate of sedimentary thickness. Uncertainties in the thickness of sediments directly affect

estimates of the inherent anisotropy of the sediments. For example, at the point shown in **Figure**

21, our reference model [*Shen et al.,* 2016] indicates a sedimentary thickness of about 4 km. If

the sediments were actually thicker, then the estimate of the inherent S-wave anisotropy would

be smaller. Uncertainty in sedimentary thickness is one of the reasons we do not highlight

structure in the basins in this paper.

6.3 Comparison with other studies

6.3.1 Vertical distribution of anisotropy in the crust

Figure 14c,d shows that the strength of inherent S-wave anisotropy is stronger in the middle-to-lower crust than in the upper crust across the study region. A comparison of **Figures 12b** and **12d** similarly shows this trend. To illustrate this trend, **Figure 22a** presents inherent S-wave anisotropy 5 km above Moho. Inherent S-wave anisotropy in the deep crust is similar to the middle crust, but stronger than the shallow crust. **Figures 18a,c, 19a,b,** and **22c** illustrate that the same trend holds for apparent radial anisotropy.

The nearly constant apparent radial anisotropy from middle to lower crust is different from the study of *Xie et al.* [2013], which concluded that apparent radial anisotropy is strongest in the middle crust. The difference between these two studies is due to two factors: (1) Love wave observations at periods below 40 sec are only weakly sensitive the shear wave speeds in the lower crust of Tibet. As a consequence, inherent S-wave anisotropy γ is poorly determined in the lowermost crust (**Fig. 8a**). (2) The study of *Xie et al.* [2013] and the current paper have different parameterization and place different constraints on anisotropy in the crust. *Xie et al.* [2013] uses the azimuthally invariant parts of Rayleigh and Love waves to invert for the apparent radial anisotropy $\hat{\gamma}$ without inferring the inherent properties, and $\hat{\gamma}$ is constrained to be 0 at the Moho. In contrast, the current study infers the inherent properties (e.g., γ, θ, Φ) from which apparent radial anisotropy $\hat{\gamma}$ is then derived. Here, we require $0 \le \gamma \le 10\%$ and the discontinuity in θ determines the resulting $\hat{\gamma}$. The result is that *Xie et al.* [2013] attempts to find a model that fits their data while minimizing lower crustal anisotropy whereas the current study applies the weak

anisotropy constraint across the entire crust. The differences between the results of these two studies illustrate that the strength of anisotropy below about 50 km depth cannot be determined by the data alone, but is shaped largely by constraints imposed in the inversion. Better determination of the amplitude of inherent S-wave anisotropy in the Tibetan lower crust will require Love wave observations at periods longer than 40 s. Such measurements will probably derive from earthquake based observations rather than ambient noise.

6.3.2 Other aspects of the model

Many studies of Tibet might meaningfully be compared with the results we present here. We briefly discuss comparisons with three general types of studies: (1) studies that have identified differences between northern and southern Tibet, (2) studies that attempt to draw conclusions about the vertical distribution of strain near the southeast border of Tibet in the Chuandian terrane or Yunnan-Guizhou plateau, and (3) receiver function studies that attempt to produce information about crustal anisotropy.

(1) Differences between northern and southern Tibet have been widely observed in other studies. Shear wave splitting studies [e.g., *McNamara et al.,* 1994; *Huang et al.,* 2000; *Hirn et al.,* 1995] find a systematic rotation of the fast azimuth from southern to northern Tibet. Compared with southern Tibet, slower shear wave speeds [e.g., *Yang et al.,* 2012] and slower Pn velocities [e.g.,*McNamara et al.,* 1997] are observed in northern Tibet. Some studies [e.g., *Huang et al.,* 2000; *Nabelek et al.,* 2009] suggest that 32°N marks the northern end of the subducted Indian plate. Although our study region only covers the eastern part of Tibet, we also observe differences between northern and southern Tibet on the western side of our study region. For example, compared with the southern part of our study region (Qiangtang terrane), the northern

part (Songpan-Ganzi) has a steeper upper crustal dip angle (**Figures 12a, 14b**) and stronger

middle crustal inherent anisotropy (**Figure 12d, 14d**).

(2) In southeastern Tibet (near the Chuandian terrane and the Yunnan-Guizhou plateau) the

deformation mechanism remains under debate. Shear wave splitting studies observe a sharp

transition in mantle anisotropy across about 25°N latitude. North of this boundary the fast

polarization orientation is mostly North-South, which is consistent with surface strain, while in

the south the fast polarization orientation changes suddenly to East-West, which deviates from

the surface strain [*Sol et al*., 2007; *Lev et al.,* 2006]. Such deviation was used as evidence for the

decoupling between the crust and mantle near the southeastern edge of Tibet because shear wave

splitting is mainly caused by mantle anisotropy.

We find a similar pattern of spatial variation in Rayleigh wave fast axis orientations in this

region. For the northern part of southeastern Tibet, Rayleigh wave fast axes are nearly constant

with period lying within about 20° of North-South (e.g., **Figure 5i** Point C), while south of 25°N

latitude the fast azimuth is more complicated. It remains oriented North-South at short periods

but changes to more nearly East-West at longer periods (e.g., **Figure 5l** Point D; **Figures 3c,d).**

In our model, the crustal strike typically follows the Rayleigh wave fast azimuth at short periods

(**Figures 3c, 13a**), and the mantle fast azimuth follows the Rayleigh wave fast azimuth at long

periods.

We tend not to attribute the different fast axis orientations between the crust and upper mantle to

decoupling between crustal and mantle strains for the following reasons. First, as pointed out by

Wang et al. [2008] and *Fouch and Rondenay* [2006], anisotropy may manifest in the crust and

mantle in very different ways for the same stress geometry. For example, crustal open cracks

might align orthogonal to the direction of maximum extension, while in the mantle the fast

direction of relatively dry olivine might align parallel to the maximum extension direction.

Secondly, the possible existence of water or melt could make the interpretation more complicated [e.g., *Kawakatsu et al.*, 2009; *Holtzman et al.*, 2003]. Moreover, as discussed in section 6.2.2 and by *Xie et al.* [2015], the Rayleigh wave fast azimuth and strike orientations of anisotropy are ambiguously related to one another if non-ellipticity of anisotropy is taken into account. Therefore, it is hazardous to draw conclusions on the coupling or decoupling of the crust and mantle deformation based on seismic anisotropy observations alone. However, *Shen et al.* [2005] argue that southeastern Tibet has a weak lower crust underlying a stronger, highly fragmented upper crust by analyzing GPS data. This could provide a possible mechanism to decouple the upper crust from the upper mantle.

(3) The tilted hexagonally symmetric (THS) model that we produce is qualitatively similar to that inferred by some receiver function studies. For example, in central Tibet, *Ozacar and Zandt* [2004] used receiver functions to study the tilt of crustal anisotropy, and found that near-surface anisotropy has a steeply dipping fabric (~60°-80°), while mid-crustal anisotropy has a shallowly dipping fabric (~18°). This result qualitatively agrees with our findings across most of eastern Tibet. In addition, the strike angles of our THS model (and the fast directions of the short period Rayleigh waves) are parallel to the fast axis orientations revealed by the Moho Ps splitting near the eastern edge of the high plateau [e.g., *Sun et al.*, 2015; *Kong et al.,* 2016]. *Sun et al.* [2015] further suggested that lower crustal flow may extrude upward into the upper crust along the steeply dipping strike faults under the Longmenshan area at the edge of the Sichuan Basin (Figure 9 in their paper), resulting in the surface uplift of the Longmenshan. Our observation of a rapid change of dip angle of the THS system from subhorizontal to subvertical beneath the same area (**Fig. 12c**) is consistent with this suggestion.

7. Summary and Conclusions

With ambient noise data recorded at CEArray, China Array, and PASSCAL stations that are located across eastern Tibet and adjacent areas, we measure Love and Rayleigh wave isotropic phase speeds and Rayleigh wave azimuthal anisotropy. In order to explain these observations jointly, we apply a method that inverts for an anisotropic medium represented by a depth-dependent tilted hexagonally symmetric (THS) elastic tensor. We perform the inversion with a Bayesian Monte Carlo method that produces depth-dependent marginal posterior distributions for the five inherent elastic moduli (A, C, N, L, and F or η) as well as dip and strike angles on a 0.5°x0.5° spatial grid. The final 3-D model is composed of the mean and standard deviation of each of these model variables.

The paper is motivated by the three questions listed in the Introduction, which are answered here. (1) Observations of apparent radial and apparent azimuthal anisotropy from surface waves can, indeed, be fit well with the oriented hexagonally symmetric elastic tensor model, analogous to the fit of similar data across the western US [*Xie et al.*, 2015]. The principal exception to this finding is that to fit the data well within the Sichuan and Qaidam basins, we would have needed to introduce very strong anisotropy into the sediments (**Fig. 21**), which was beyond the scope of this paper. (2) In contrast to results in the western US, we find that the data across much of the study region could not be fit with a single orientation for the elastic tensor at all depths in the crust. Specifically, we find that two dip angles (one in the upper crust and the other in the middle to lower crust) are needed in Tibet and the Yunnan-Guizhou plateau. However, a single strike angle in the crust does suffice to allow the data to be fit near the periphery of Tibet. (3) The vertical distribution of anisotropy within Tibet is similar to that beneath the Yunnan-Guizhou plateau, but both regions differ from the periphery of Tibet where only a single dip angle is need.

Our results, therefore, segregate the area of study into two regions based on crustal anisotropy. Region 1 includes the interior of eastern Tibet and the Yunnan-Guizhou plateau. In this region, steeply dipping upper crust overlies shallowly dipping middle to lower crust and inherent S-wave anisotropy γ (eqn. (5)) is strong throughout the crust with larger amplitudes in the middle-to-lower crust. As a result, the apparent radial anisotropy $\hat{\gamma}$ (eqn. (6)) and apparent azimuthal anisotropy $\hat{\Gamma}$ (eqn. (7)) bifurcate vertically. $\hat{\gamma}$ tends to be weak and negative in the upper crust and is strong and positive in the middle-to-lower crust while $\hat{\Gamma}$ is strong mostly in the upper crust. The steep dip to the symmetry axis in the upper crust may result from fractures or faults that are sub-vertical or steeply dipping. In contrast, the sub-horizontal or shallow dipping symmetry axes in the middle-to-lower crust may result from ductile deformation that aligns the orientation of anisotropic minerals such as mica. Region 2 covers the edge of eastern Tibet and regions north of Tibet where the foliation across entire crust has a moderate to steep dip angle and inherent S-wave anisotropy γ does not change strongly with depth. As a result, apparent radial anisotropy $\hat{\gamma}$ is negative to slightly positive through the entire crust, and apparent azimuthal anisotropy $\hat{\Gamma}$ is strong throughout the crust. The more steeply dipping foliation planes may be caused by the reorientation of anisotropic minerals as crustal flows rotate and shear near the border of Tibet, which may result from resistance forces imposed by the more rigid and relatively undeformed surroundings to Tibet.

In the future, the introduction of other data sets may improve the current inversion, which is based exclusively on surface waves from ambient noise. Such information could provide new insight into crustal and mantle deformation and the generation of more realistic petrologic models that agree with the elastic tensors inferred. (1) Azimuthal variations in receiver functions

(e.g., *Levin and Park, 1997,1998*; *Ozacar and Zandt, 2004; 2009*; *Schulte-Pelkum and Mahan, 2014a,b*) as well as the splitting of the P-to-S converted phase (e.g., *Rumpker et al., 2014*; *Sun et al., 2015a*) can provide important point constraints on crustal anisotropy and could also help to identify depths at which crustal anisotropy changes dip angle. In some areas receiver function waveforms observe clear azimuthal variations, and these waveforms could be inverted simultaneously for the layered THS system [e.g., *Ozacar and Zandt et al.*, 2004; *Schulte-Pelkum and Mahan*, 2014a] together with surface wave data. (2) Rayleigh wave H/V ratio provides sensitivity to the velocity structure at shallow depths (upper ~5km), and would help to resolve anisotropy in the sedimentary basins. (3) Shear wave splitting, both SKS and the splitting of Moho converted P-to-S phases, could be combined with surface wave data to provide additional constraints on the depth-integrated amplitude of apparent azimuthal anisotropy [e.g., *Lin et al.*, 2010; *Montagner* et al., 2000]. (4) In addition, longer period surface wave measurements are needed to improve estimates of mantle anisotropy, including the type of anisotropy (e.g., hexagonal symmetry with a fast or slow symmetry axis, orthorhombic symmetry) and the orientation of the anisotropic media.

1
2
3
4
5
6
7
8
9
10
11
12
13
14
15
16
17
18
19
20
21
22
23
24
25
26
27
28
29
30
31
32
33
34
35
36
37
38
39
40
41
42
43
44
45
46
47
48
49
50
51
52
53
54
55
56
57
58
59
60

1
2
3
4
5
6
7
8
9
10
11
12
13
14
15
16
17
18
19
20
21
22
23
24
25
26
27
28
29
30
31
32
33
34
35
36
37
38
39
40
41
42
43
44
45
46
47
48
49
50
51
52
53
54
55
56
57
58
59
60
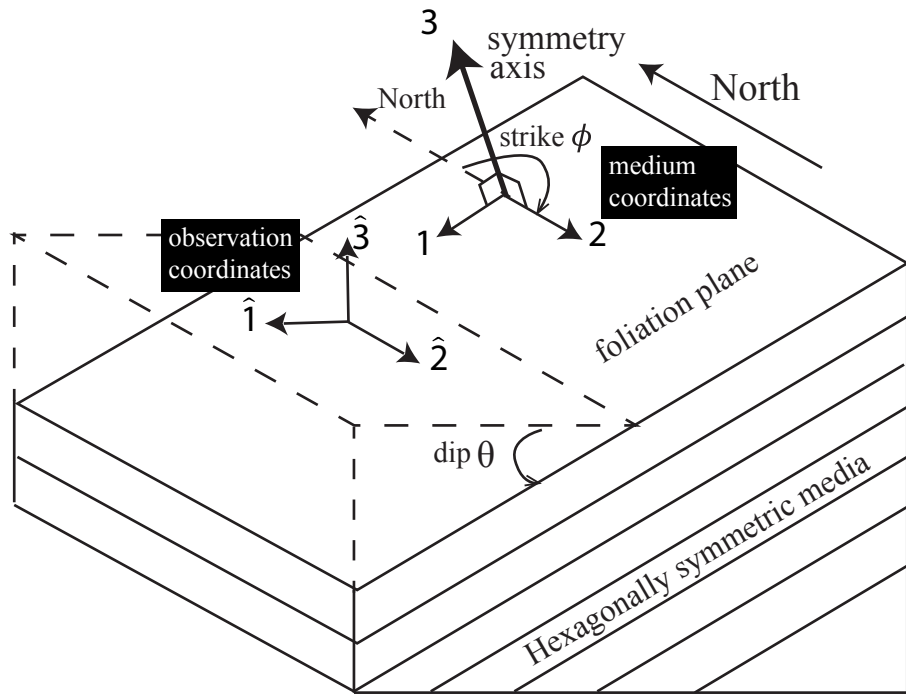
Figure 1. Depiction of a tilted hexagonally symmetric medium (THS), showing the foliation plane, the strike and dip angles, and the symmetry axis. The medium coordinates (x_1, x_2, x_3) and the observing coordinates ($\hat{x}_1, \hat{x}_2, \hat{x}_3$) are also shown.
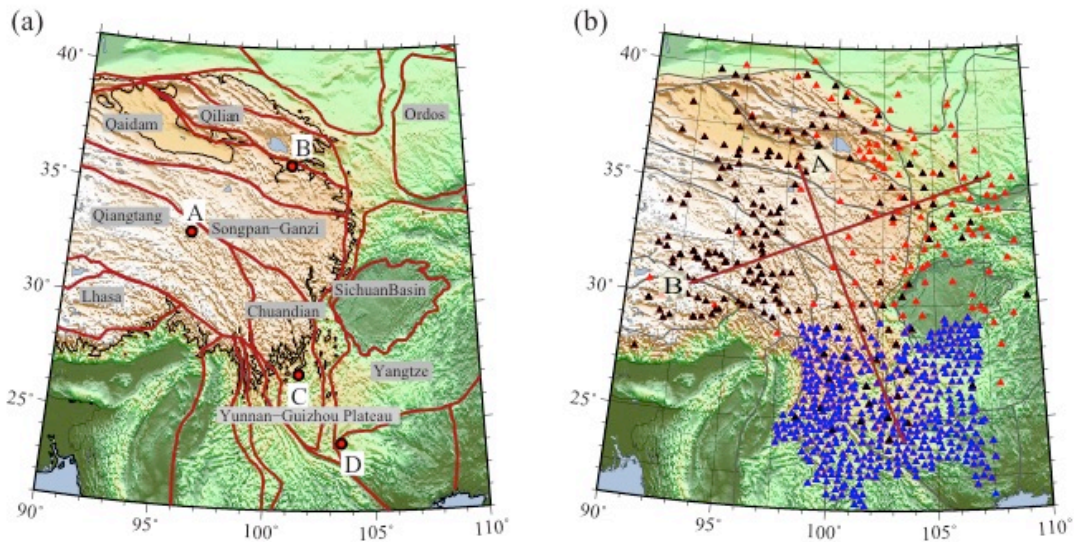
Figure 2. (a) Reference map of the study region in which 3 km topography isolines are presented (black lines) along with the boundaries of major geological units (red lines). Points A - D indicate sample locations referenced in **Figs. 5, 8-11, 17,** and **21**. (b) Locations of seismic stations used in this study: CEArray stations (red triangles), China Array stations around Yunnan province (blue triangles), and PASSCAL stations (black triangle). The two profiles (A, B) are used in **Figs. 14** and **19**.
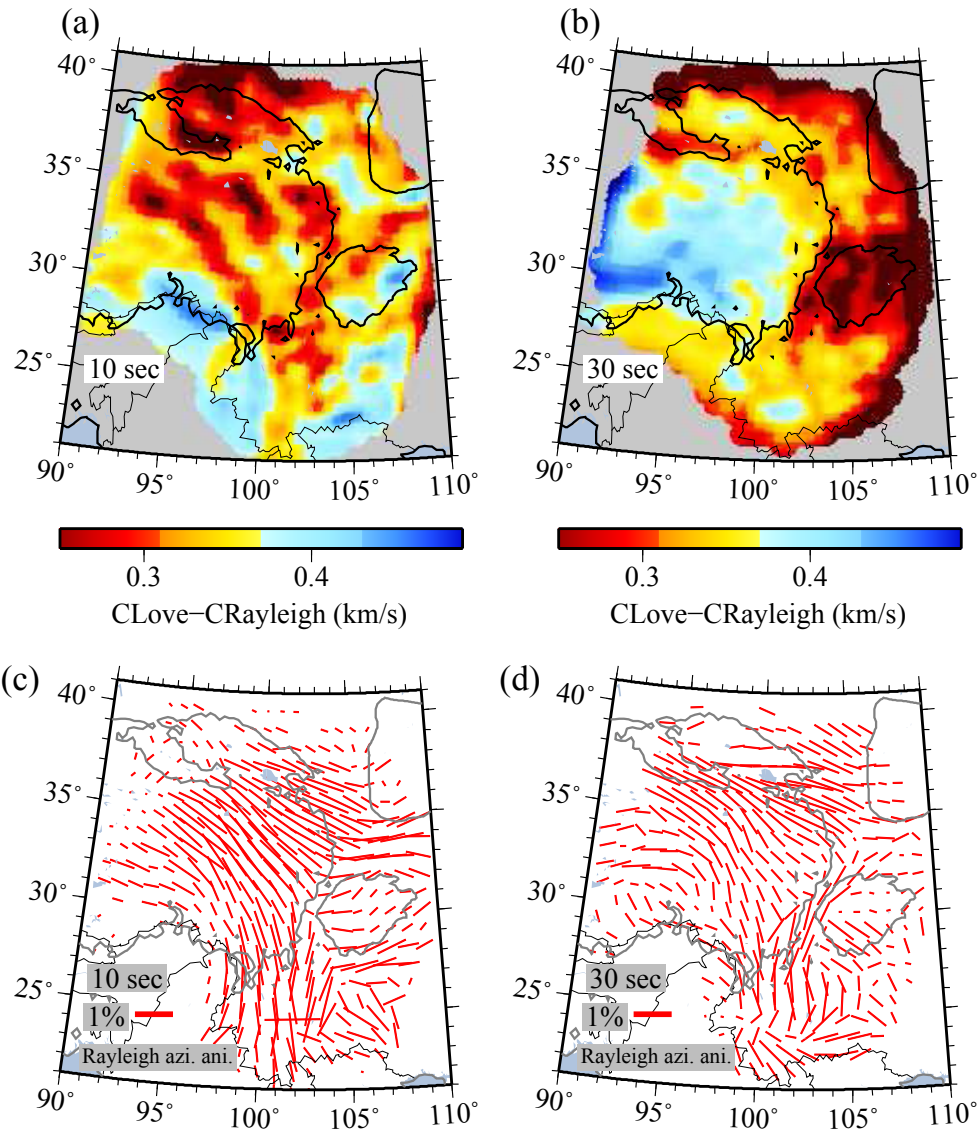
Figure 3. (a, b) Examples of the Love-Rayleigh phase speed difference ($C_{Love} - C_{Rayleigh}$) across the study region at periods of 10 and 30 sec. (c, d) The observed Rayleigh wave 2ψ (180° periodicity) azimuthal anisotropy maps at 10 and 30 sec periods. The red bars identify Rayleigh wave fast orientations with lengths proportional to the amplitude in percent (a_2 in eqn. (1)).
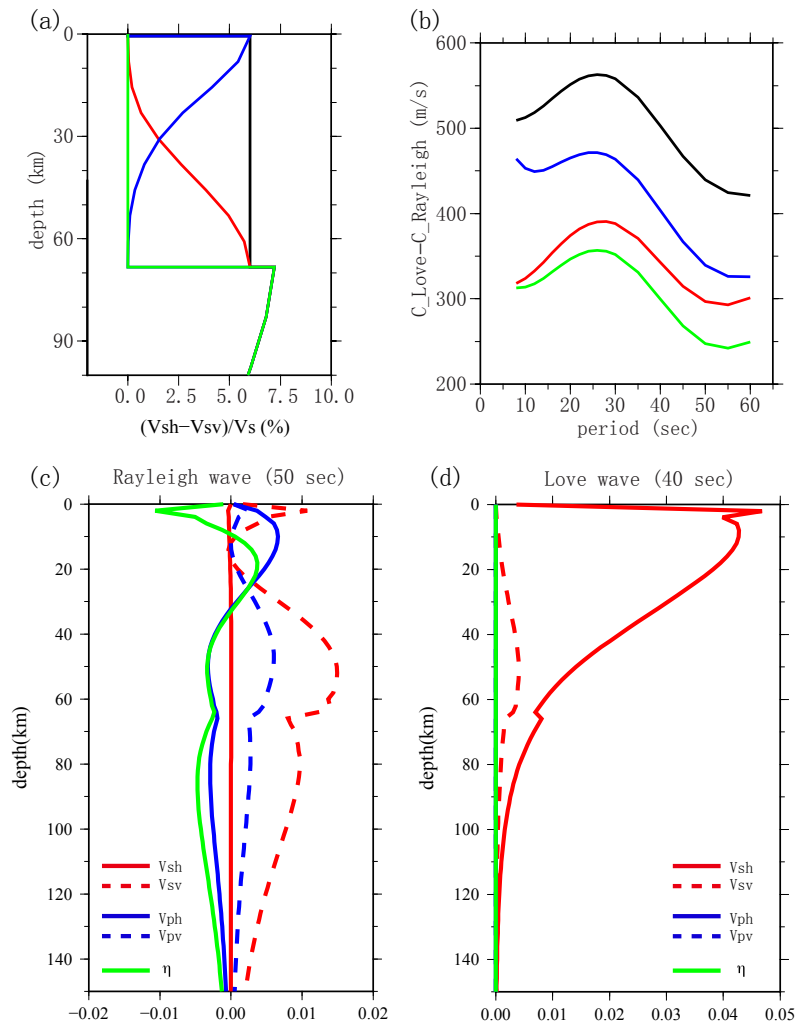
Figure 4. (a, b) Simulations that illustrate the effect of changes in a hexagonally symmetric medium with a vertical symmetry axis (VHS medium) on the Love-Rayleigh phase speed difference. (a) Four types of structures with different amplitudes of radial anisotropy ($V_{SH} - V_{SV}$ in %) in the crust. (b) The Love-Rayleigh phase speed differences ($C_{Love} - C_{Rayleigh}$) computed from the structures shown in (a). (c, d) Example sensitivity kernels for Rayleigh and Love wave phase velocities for a VHS medium: 50 s period for Rayleigh waves with perturbations in Vsv, Vsh, Vpv, Vph, and η, as a function of depth, and 40 s period for Love waves with perturbations in Vsh and Vsv.
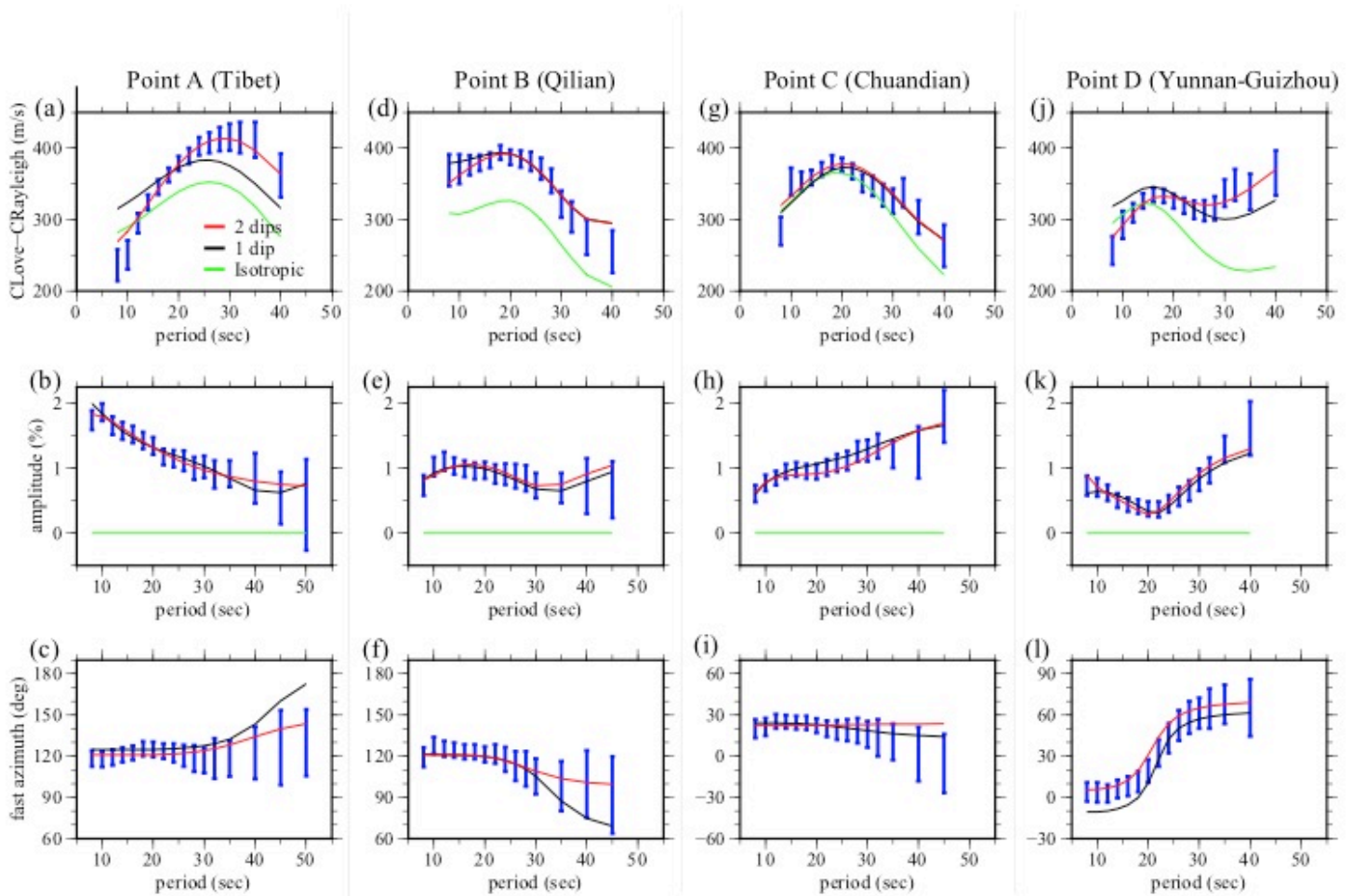
Figure 5. Surface wave measurements presented as 1σ error bars illustrating model fits at four locations: eastern Tibet (Point A), Qilian terrane (Point B), Chuandian terrane (Point C), and Yunan-Guizhou plateau (Point D) identified in **Fig. 2a**. (a,d,g,j) Love minus Rayleigh wave phase speed. (b,e,h,k) Amplitude of Rayleigh wave azimuthal anisotropy (coefficient a_2 in eqn. (1)). (c,f,i,l) Rayleigh wave fast axis orientation. The solid lines are curves computed from the best fitting model at the location using three model parameterizations: isotropic model (green lines), tilted hexagonally symmetric (THS) model with a constant dip angle in the crust (black lines), and THS model with two dip angles in the crust (red lines). Aspects of the THS models with two crustal dip angles are shown in **Fig. 11**.
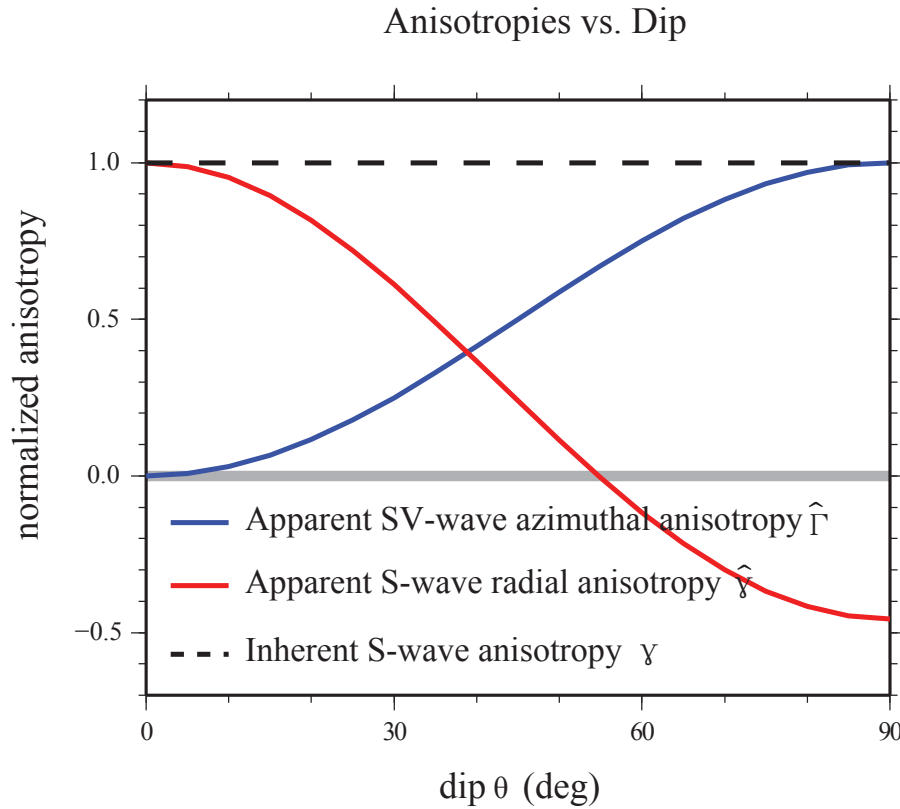
Figure 6. Variation of apparent S-wave radial anisotropy $\hat{\gamma}$ (red curve) and apparent SV-wave azimuthal anisotropy $\hat{\Gamma}$ (blue curve) as a function of dip angle θ. The inherent S-wave anisotropy γ is constant and normalized to unity. This computation results from a simplified hexagonally symmetric elastic tensor, details of these functions will depend on the form of the elastic tensor.
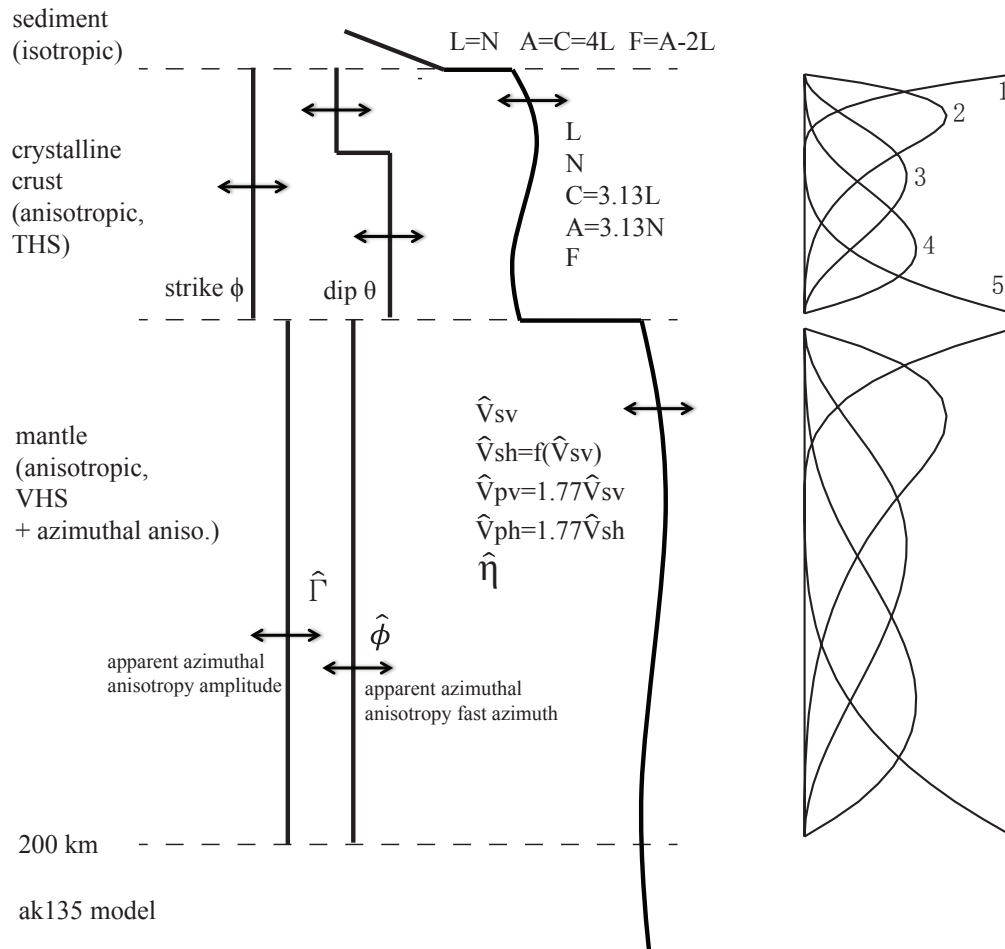
Figure 7. Model parameterization. Sedimentary structure is isotropic with shear and compressional velocities increasing linearly with depth. The crystalline crust is an anisotropic THS medium described by seven depth-dependent parameters: five inherent elastic moduli, dip angle, and strike angle. The elastic moduli change smoothly with depth and are represented with five B-splines. Strike is constant within the crystalline crust and dip is allowed to change once within the crystalline crust at a depth of one-third of the crustal thickness. The uppermost mantle is modeled as a VHS anisotropic medium plus apparent azimuthal anisotropy and is described by seven parameters: five apparent elastic moduli ($\hat{V}_{SV}, \hat{V}_{SH}, \hat{V}_{PV}, \hat{V}_{PH}, \hat{\eta}$) and two parameters to represent apparent azimuthal anisotropy ($\hat{\Gamma}, \hat{\phi}$). Mantle apparent radial anisotropy $\hat{\gamma}$ is constrained to be 4.5% and the amplitude of mantle apparent azimuthal anisotropy is constant with depth.
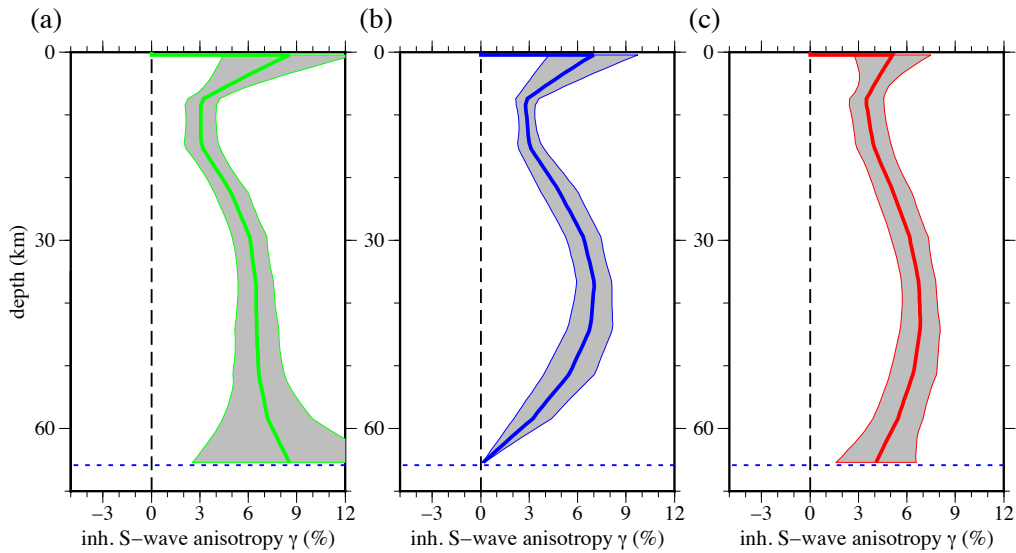
Figure 8. Mean (solid colored lines) and standard deviation (grey corridor) of posterior distributions of inherent S-wave anisotropy (γ) at Point A in Tibet showing the vertical variation of this quantity with different constraints applied in the inversion: (a) $\gamma \geq 0$ across the crust, (b) $\gamma \geq 0$ across the crust but γ is set to 0 at the base of the crust, similar to *Xie et al.* (2013); and (c) $0 \leq \gamma \leq 10\%$ across the entire crust as done in this paper. γ is not well constrained by our observations below 50 km depth.
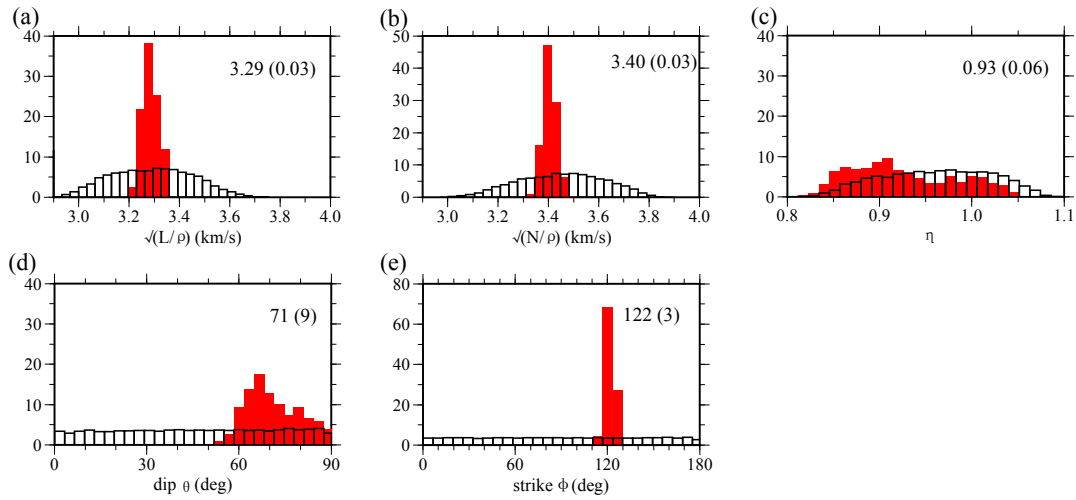
Figure 9. Example comparison of prior and posterior marginal distributions from the Bayesian Monte Carlo inversion for five example model parameters at 10 km depth for Point A in Tibet (**Fig. 2a**). White histograms are the prior marginal distributions and red histograms are the posterior marginal distributions. The average and standard deviation of the posterior distributions are presented on each plot.
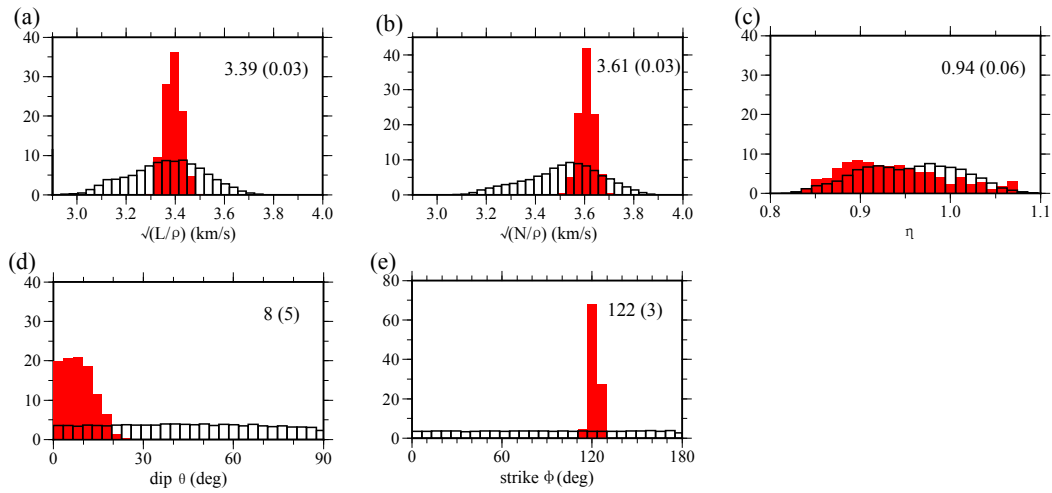
Figure 10. Similar to **Fig. 9**, but at 30 km depth, again for Point A in Tibet.

1
2
3
4
5
6
7
8
9
10
11
12
13
14
15
16
17
18
19
20
21
22
23
24
25
26
27
28
29
30
31
32
33
34
35
36
37
38
39
40
41
42
43
44
45
46
47
48
49
50
51
52
53
54
55
56
57
58
59
60
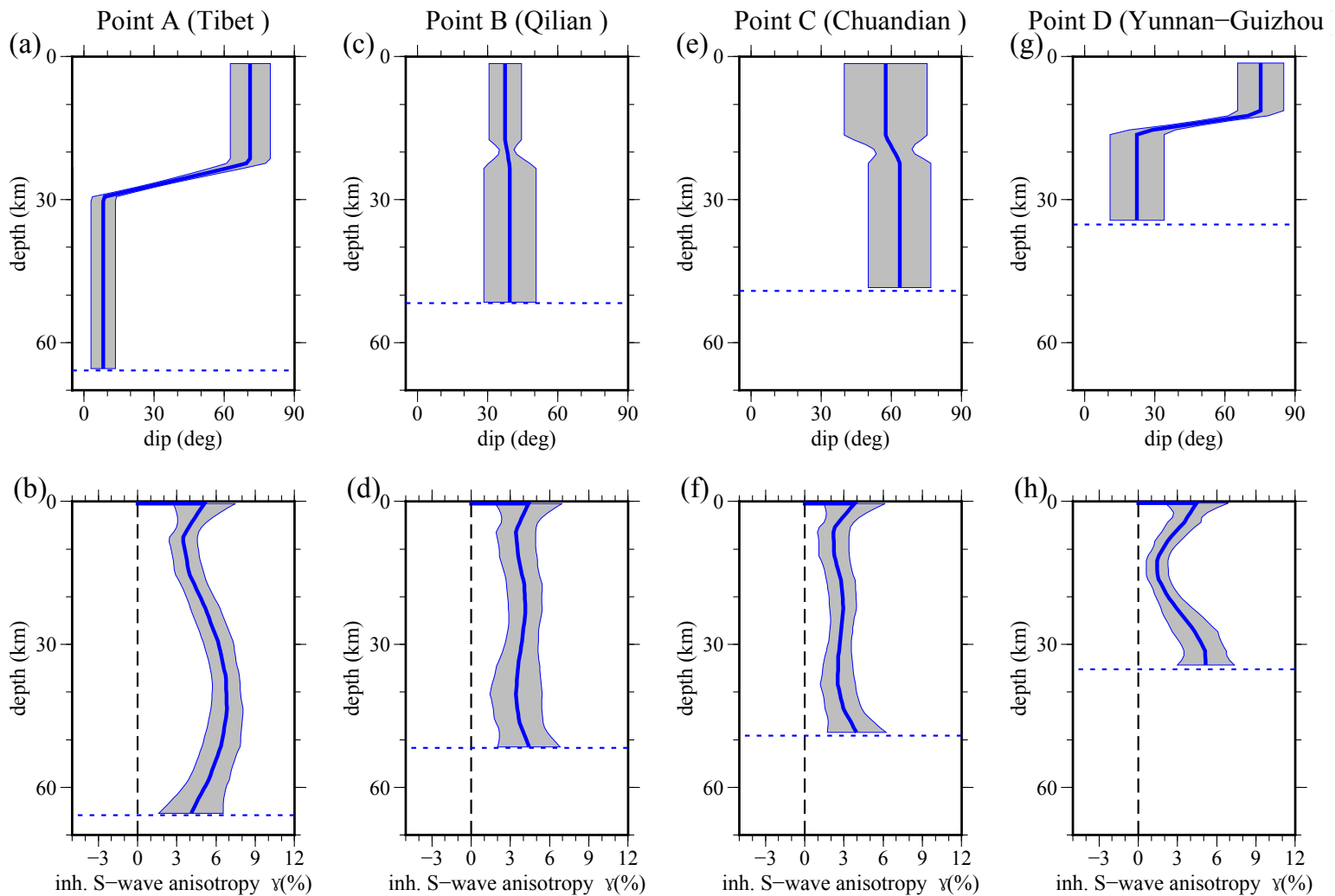
Figure 11. Posterior distributions of inherent anisotropic variables at Points A –D (**Fig. 2a**) showing (a,c,e,g) the vertical variation of the dip angle θ and (b,d,f,h) the inherent S-wave anisotropy γ . The one-standard deviation extent of the posterior distribution is shown at each depth with the grey corridor and the average is plotted with bold black solid lines. Only the crystalline crustal part of the model is shown because sediments are isotropic and the mantle is parameterized in terms of apparent moduli, so no inherent property is inferred.
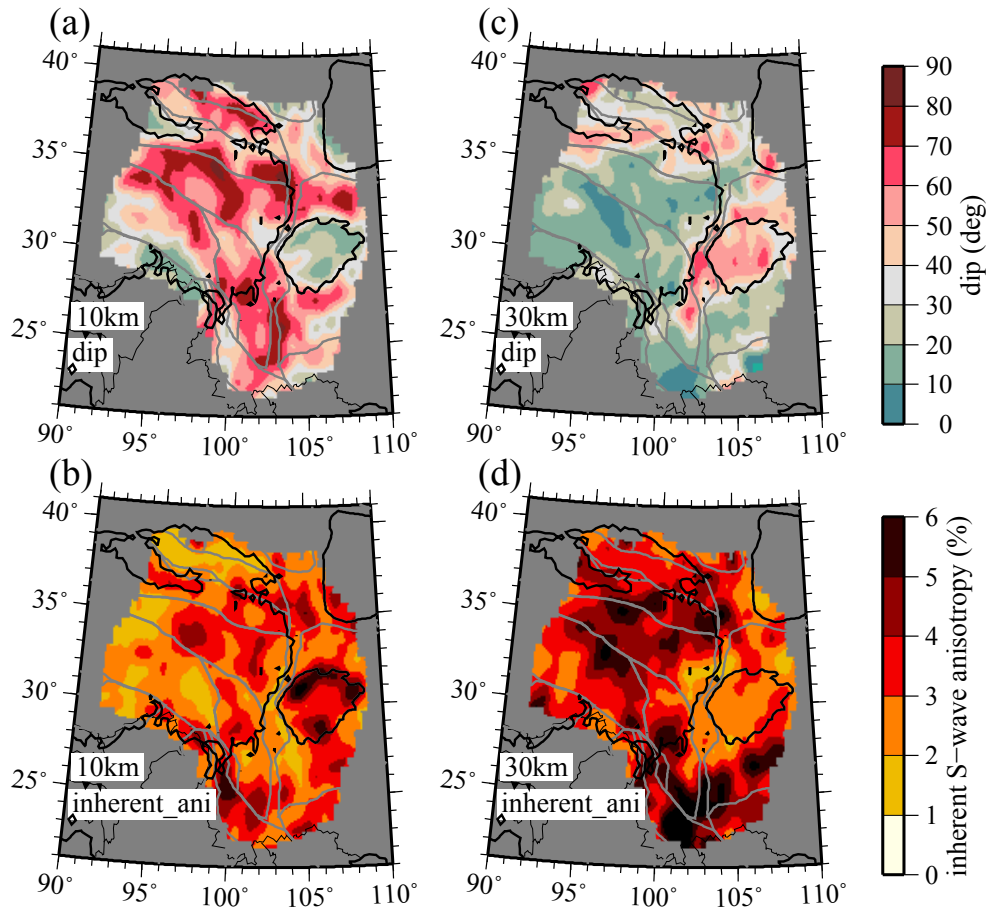
Figure 12. Map views of the dip angle θ and inherent S-wave anisotropy γ, respectively, at depths of: (a, b) 10 km and (c, d) 30 km.
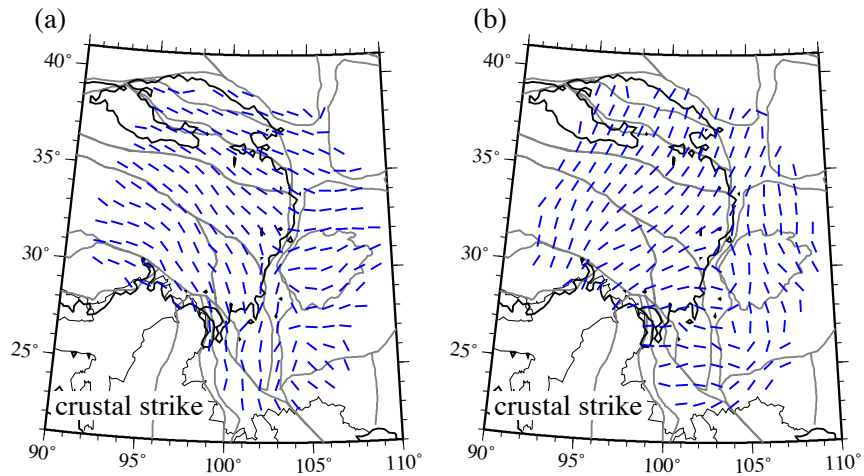
Figure 13. (a) The orientation of the local crustal strike angle ϕ determined here, which is constant vertically throughout the crust, is shown with blue bars. (b) Crustal strike orientation perpendicular to the results shown in (a), acknowledging the ambiguity in the estimate of the crustal strike angle.
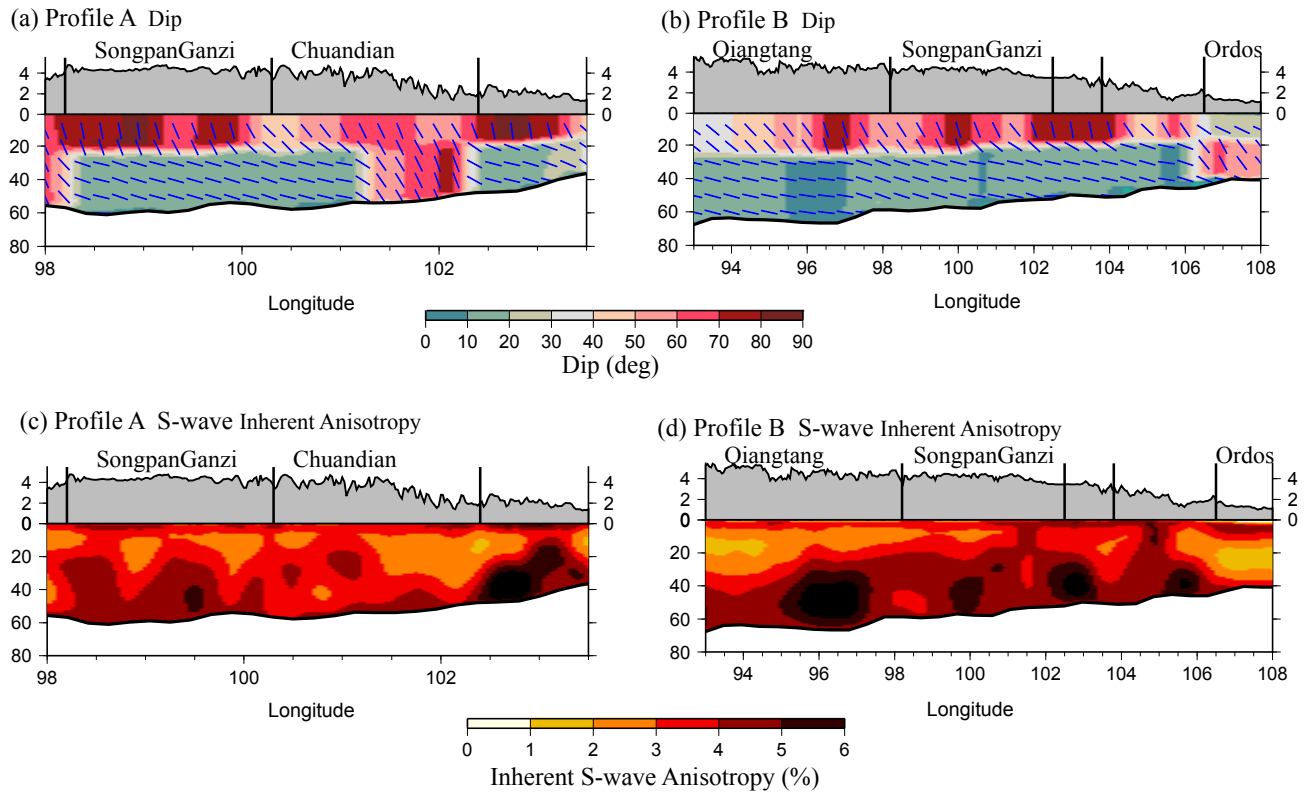
Figure 14. Vertical transects of inherent S-wave anisotropy γ and dip angle θ along profiles A and B identified in **Fig. 2b**. In (a) and (b) dip angle is color-coded and the orientation of the foliation plane is presented with short blue bars. In (c) and (d), γ is color-coded in percent. Only the crustal part of the model is presented because the mantle is parameterized in terms of apparent moduli.
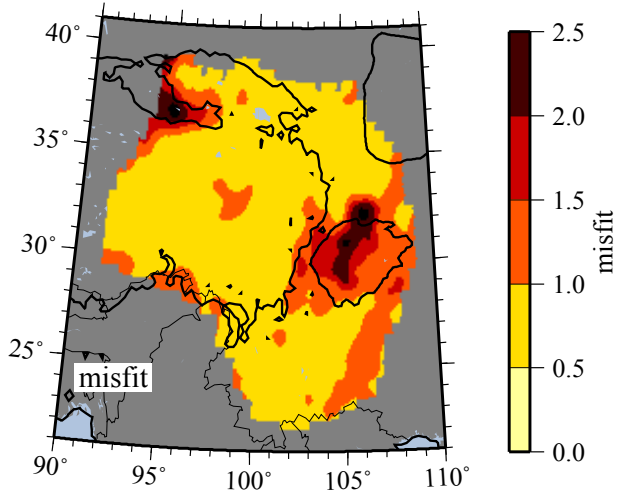
Figure 15. Geographic variation in data misfit produced by the best-fitting model at each location. Misfit is defined as the square root of the reduced chi-squared value at each location (eqn. (8)).
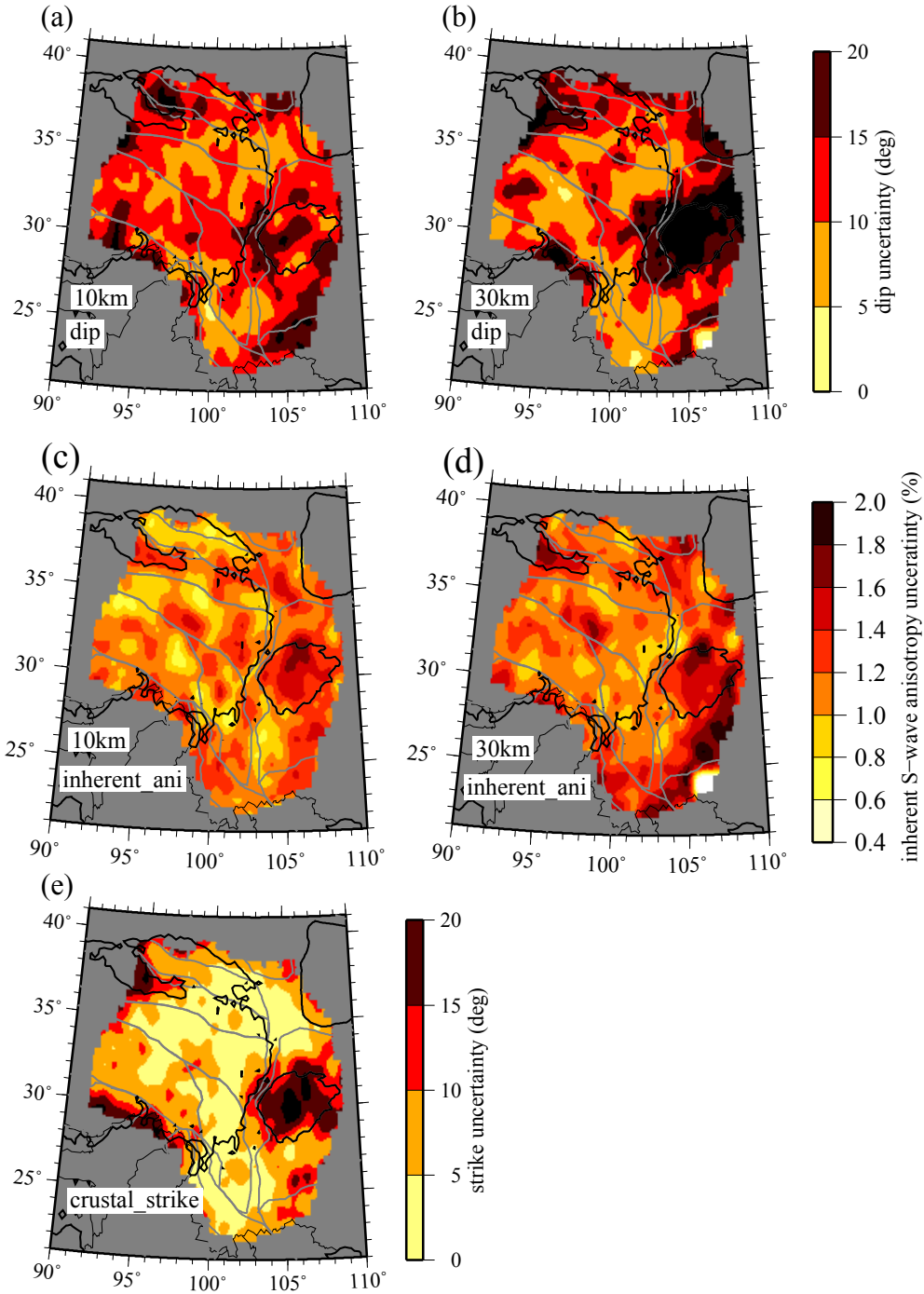
Figure 16. Map views of the standard deviation of the posterior distribution for (a,b) dip angle θ and (c,d) inherent S-wave anisotropy γ at depths of 10 km and 30 km, respectively. (e) Standard deviation of the posterior distribution for strike angle, which is constant in the crust.
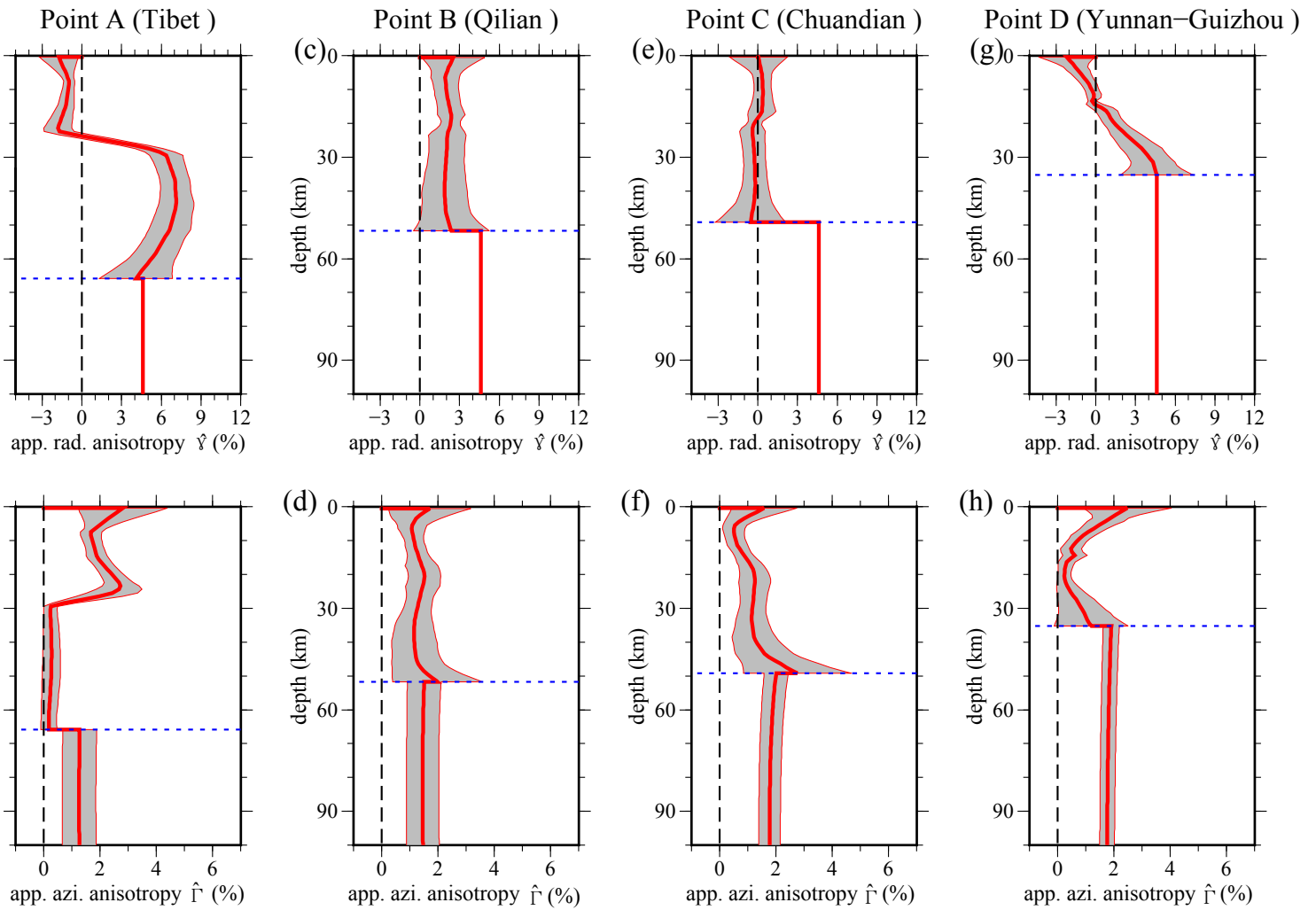
Figure 17. Posterior distributions of apparent radial ($\hat{\gamma}$) and apparent azimuthal ($\hat{\Gamma}$) anisotropy defined similarly to **Fig. 11** for comparison.
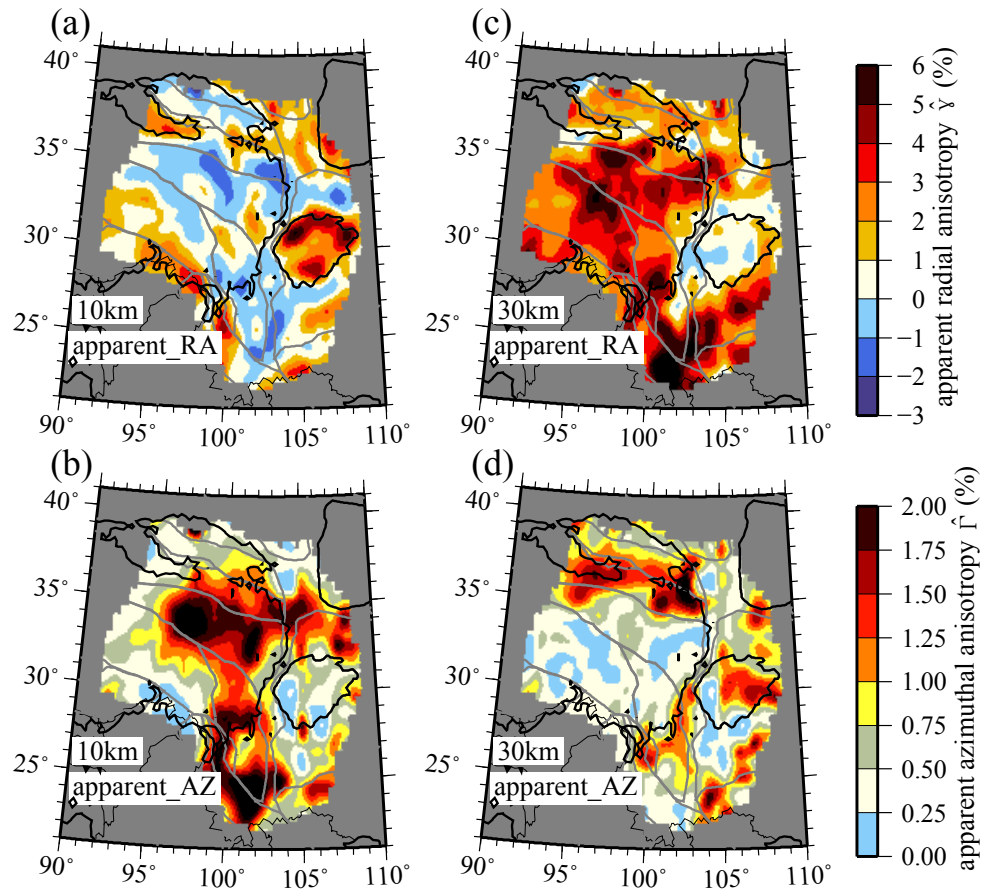
Figure 18. Map views of apparent radial ($\hat{\gamma}$) and apparent azimuthal ($\hat{\Gamma}$) anisotropy defined similarly to **Fig. 12** for comparison.
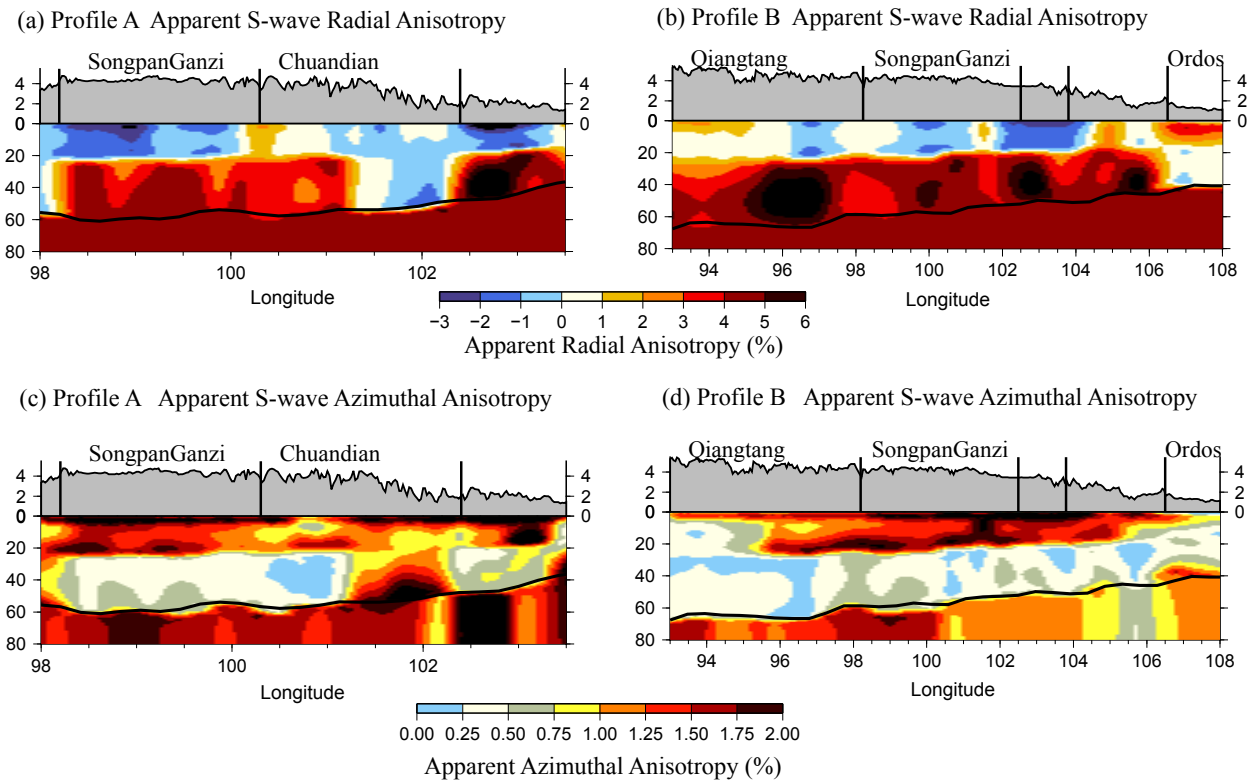
Figure 19. Vertical transects of apparent radial ($\hat{\gamma}$) and apparent azimuthal ($\hat{\Gamma}$) anisotropy defined similarly to **Fig. 14** for comparison.
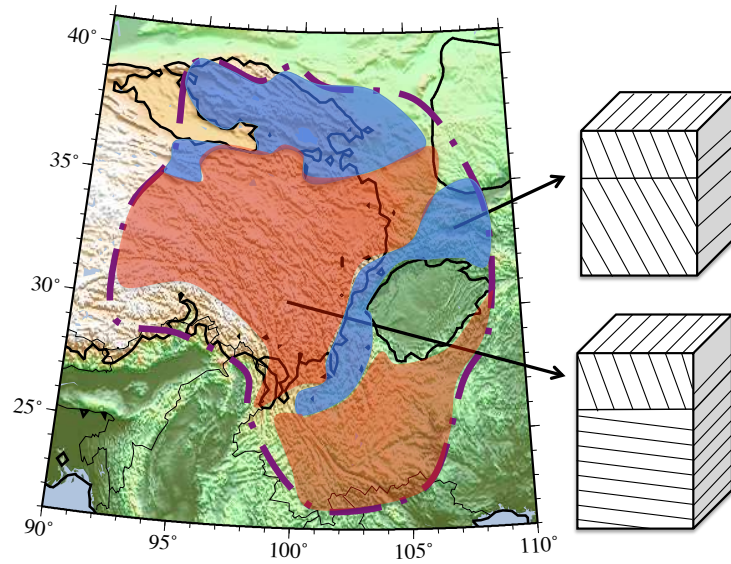
Figure 20. Regionalization of anisotropy in the final 3-D model. The dashed line indicates the study region. The blue shaded regions are characterized by moderately to steeply dipping foliations throughout the entire crust. The red shaded regions have foliations dipping steeply in the upper crust overlying a sub-horizontally foliated middle-to-lower crust.
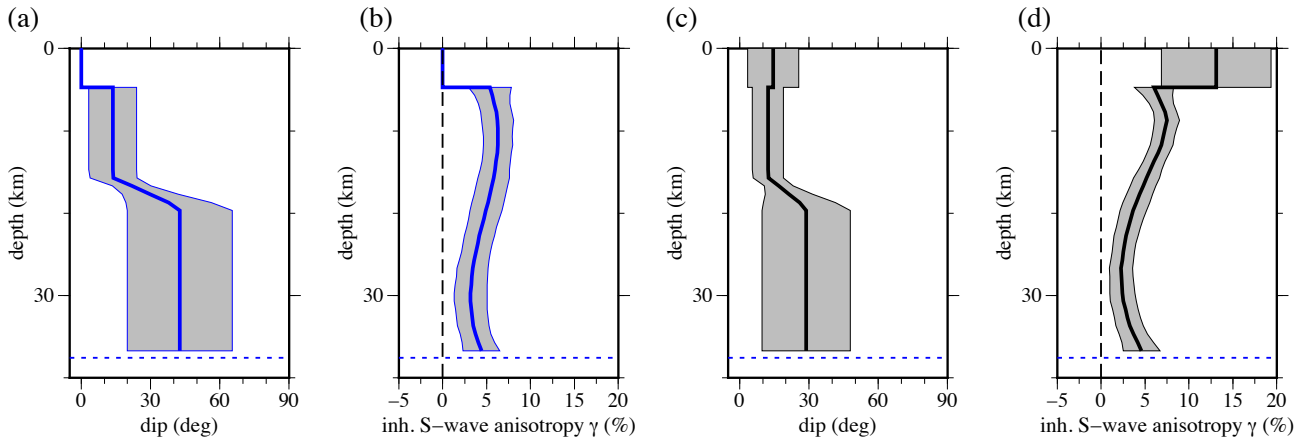
Figure 21. (a-b) Posterior distributions of estimated dip angle θ and inherent S-wave anisotropy γ for a point in the Sichuan basin (105°, 31°) presented as in **Fig. 11** with no anisotropy in the sediments. (c-d) Posterior distributions at the same location where anisotropy and an independent dip angle is allowed in the sediments.
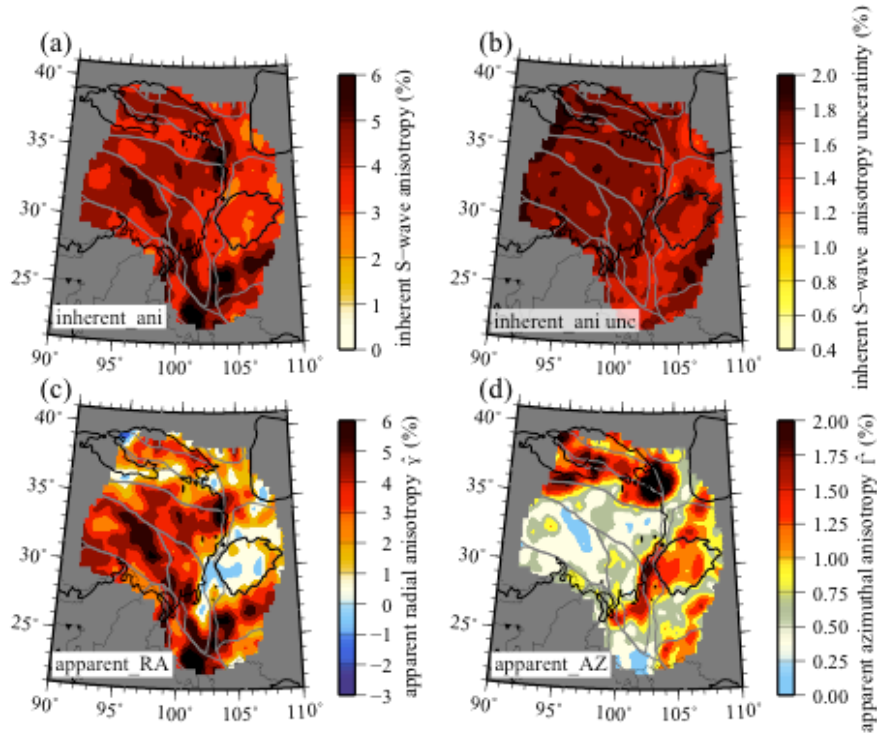
Figure 22. Aspects of inherent and apparent anisotropy estimated at a depth 5 km above the Moho: (a) inherent S-wave anisotropy γ, (b) standard deviation of the posterior distribution for γ, (c) apparent radial anisotropy $\hat{\gamma}$, and (d) apparent azimuthal anisotropy $\hat{\Gamma}$.

References:

Acton, C. E., K. Priestley, V. K. Gaur, and S. S. Rai (2010), Group velocity tomography of the Indo-Eurasian collision zone, *J. Geophys. Res. Solid Earth*, *115*(B12), B12335, doi:10.1029/2009JB007021.

Agius, M. R., and S. Lebedev (2014), Shear-velocity structure, radial anisotropy and dynamics of the Tibetan crust, *Geophys. J. Int.*, *199*(3), 1395–1415, doi:10.1093/gji/ggu326.

Auld, B. A. (1973), *Acoustic fields and waves in solids*, Wiley.

Barmin, M. P., M. H. Ritzwoller, and A. L. Levshin (2001), A Fast and Reliable Method for Surface Wave Tomography, *Pure Appl. Geophys.*, *158*(8), 1351–1375, doi:10.1007/PL00001225.

Beaumont, C., R. A. Jamieson, M. H. Nguyen, and B. Lee (2001), Himalayan tectonics explained by extrusion of a low-viscosity crustal channel coupled to focused surface denudation, *Nature*, *414*(6865), 738–742, doi:10.1038/414738a.

Bensen, G. D., M. H. Ritzwoller, M. P. Barmin, A. L. Levshin, F. Lin, M. P. Moschetti, N. M. Shapiro, and Y. Yang (2007), Processing seismic ambient noise data to obtain reliable broad-band surface wave dispersion measurements, *Geophys. J. Int.*, *169*(3), 1239–1260, doi:10.1111/j.1365-246X.2007.03374.x.

Bollinger, L., P. Henry, and J. Avouac (2006), Mountain building in the Nepal Himalaya: Thermal and kinematic model, *Earth Planet. Sci. Lett.*, *244*(1-2), 58–71, doi:10.1016/j.epsl.2006.01.045.

Brownlee, S. J., B. R. Hacker, M. Salisbury, G. Seward, T. A. Little, S. L. Baldwin, and G. A. Abers (2011), Predicted velocity and density structure of the exhuming Papua New Guinea ultrahigh-pressure terrane, *J. Geophys. Res. Solid Earth*, *116*(B8), B08206, doi:10.1029/2011JB008195.

Caldwell, W. B., S. L. Klemperer, S. S. Rai, and J. F. Lawrence (2009), Partial melt in the upper-middle crust of the northwest Himalaya revealed by Rayleigh wave dispersion, *Tectonophysics*, *477*(1–2), 58–65, doi:10.1016/j.tecto.2009.01.013.

Carcione, J. J. M. (2007), *Wave Fields in Real Media: Wave Propagation in Anisotropic, Anelastic, Porous and Electromagnetic Media*, Elsevier.

Chen, Y., J. Badal, and Z. Zhang (2009), Radial anisotropy in the crust and upper mantle beneath the Qinghai-Tibet Plateau and surrounding regions, *J. Asian Earth Sci.*, *36*(4–5), 289–302, doi:10.1016/j.jseaes.2009.06.011.

Christensen, N. I. (1984), The magnitude, symmetry and origin of upper mantle anisotropy based on fabric analyses of ultramafic tectonites, *Geophys. J. Int.*, *76*(1), 89–111, doi:10.1111/j.1365-246X.1984.tb05025.x.

Chu, R., L. Zhu, and D. V. Helmberger (2009), Determination of earthquake focal depths and source time functions in central Asia using teleseismic P waveforms, *Geophys. Res. Lett.*, *36*, doi:10.1029/2009GL039494.

Clark, M. K., and L. H. Royden (2000), Topographic ooze: Building the eastern margin of Tibet by lower crustal flow, *Geology*, *28*(8), 703–706, doi:10.1130/0091-7613(2000)28<703:TOBTEM>2.0.CO;2.

Copley, A., J.-P. Avouac, and B. P. Wernicke (2011), Evidence for mechanical coupling and strong Indian lower crust beneath southern Tibet, *Nature*, *472*(7341), 79–81, doi:10.1038/nature09926.

Cotte, N., H. Pedersen, M. Campillo, J. Mars, J. F. Ni, R. Kind, E. Sandvol, and W. Zhao (1999), Determination of the crustal structure in southern Tibet by dispersion and amplitude analysis of Rayleigh waves, *Geophys. J. Int.*, *138*(3), 809–819, doi:10.1046/j.1365-246x.1999.00927.x.

Crampin, S. (1984), Effective anisotropic elastic constants for wave propagation through cracked solids, *Geophys. J. Int.*, *76*(1), 135–145, doi:10.1111/j.1365-246X.1984.tb05029.x.

Deng, Q., P. Zhang, Y. Ran, X. Yang, W. Min, and Q. Chu (2003), Basic characteristics of active tectonics of China, *Sci. China Ser. Earth Sci.*, *46*(4), 356–372, doi:10.1360/03yd9032.

Deng, Y., W. Shen, T. Xu, and M. H. Ritzwoller (2015), Crustal layering in northeastern Tibet: a case study based on joint inversion of receiver functions and surface wave dispersion, *Geophys. J. Int.*, *203*(1), 692–706, doi:10.1093/gji/ggv321.

Duret, F., N. M. Shapiro, Z. Cao, V. Levin, P. Molnar, and S. Roecker (2010), Surface wave dispersion across Tibet: Direct evidence for radial anisotropy in the crust, *Geophys. Res. Lett.*, *37*(16), L16306, doi:10.1029/2010GL043811.

England, P., and P. Molnar (1997), Active deformation of Asia: From kinematics to dynamics, *Science*, *278*(5338), 647–650, doi:10.1126/science.278.5338.647.

Erdman, M. E., B. R. Hacker, G. Zandt, and G. Seward (2013), Seismic anisotropy of the crust: electron-backscatter diffraction measurements from the Basin and Range, *Geophys. J. Int.*, *195*(2), 1211–1229, doi:10.1093/gji/ggt287.

Fouch, M. J., and S. Rondenay (2006), Seismic anisotropy beneath stable continental interiors, *Phys. Earth Planet. Inter.*, *158*(2–4), 292–320, doi:10.1016/j.pepi.2006.03.024.

Francheteau, J., C. Jaupart, S. X. Jie, K. Wen-Hua, L. De-Lu, B. Jia-Chi, W. Hung-Pin, and D. Hsia-Yeu (1984), High heat flow in southern Tibet, *Nature*, *307*(5946), 32–36, doi:10.1038/307032a0.

French, S. W., and B. A. Romanowicz (2014), Whole-mantle radially anisotropic shear velocity structure from spectral-element waveform tomography, *Geophys. J. Int.*, *199*(3), 1303–1327, doi:10.1093/gji/ggu334.

Guo, Z., X. Gao, H. Yao, J. Li, and W. Wang (2009), Midcrustal low-velocity layer beneath the central Himalaya and southern Tibet revealed by ambient noise array tomography, *Geochem. Geophys. Geosystems*, *10*(5), Q05007, doi:10.1029/2009GC002458.

Guo, Z., X. Gao, W. Wang, and Z. Yao (2012), Upper- and mid-crustal radial anisotropy beneath the central Himalaya and southern Tibet from seismic ambient noise tomography, *Geophys. J. Int.*, *189*(2), 1169–1182, doi:10.1111/j.1365-246X.2012.05425.x.

Hacker, B. R., M. H. Ritzwoller, and J. Xie (2014), Partially melted, mica-bearing crust in Central Tibet, *Tectonics*, *33*(7), 2014TC003545, doi:10.1002/2014TC003545.

Hirn, A. et al. (1995), Seismic anisotropy as an indicator of mantle flow beneath the Himalayas and Tibet, *Nature*, *375*(6532), 571–574, doi:10.1038/375571a0.

Holtzman, B. K., D. L. Kohlstedt, M. E. Zimmerman, F. Heidelbach, T. Hiraga, and J. Hustoft (2003), Melt Segregation and Strain Partitioning: Implications for Seismic Anisotropy and Mantle Flow, *Science*, *301*(5637), 1227–1230, doi:10.1126/science.1087132.

Houseman, G., and P. England (1993), Crustal thickening versus lateral expulsion in the Indian-Asian continental collision, *J. Geophys. Res. Solid Earth*, *98*(B7), 12233–12249, doi:10.1029/93JB00443.

Huang, H., H. Yao, and R. D. van der Hilst (2010), Radial anisotropy in the crust of SE Tibet and SW China from ambient noise interferometry, *Geophys. Res. Lett.*, *37*, 5 PP., doi:201010.1029/2010GL044981.

Huang, W.-C. et al. (2000), Seismic polarization anisotropy beneath the central Tibetan Plateau, *J. Geophys. Res. Solid Earth*, *105*(B12), 27979–27989, doi:10.1029/2000JB900339.

Jiang, M., S. Zhou, E. Sandvol, X. Chen, X. Liang, Y. J. Chen, and W. Fan (2011), 3-D lithospheric structure beneath southern Tibet from Rayleigh-wave tomography with a 2-D seismic array, *Geophys. J. Int.*, *185*(2), 593–608, doi:10.1111/j.1365-246X.2011.04979.x.

Jolivet, L., P. Davy, and P. Cobbold (1990), Right-lateral shear along the Northwest Pacific Margin and the India-Eurasia Collision, *Tectonics*, *9*(6), 1409–1419, doi:10.1029/TC009i006p01409.

Kang, D., W. Shen, J. Ning, and M. H. Ritzwoller (2015), Seismic evidence for lithospheric modification associated with intracontinental volcanism in Northeastern China, *Geophys. J. Int.*, *204*(1), 215–235, doi:10.1093/gji/ggv441.

Kawakatsu, H., P. Kumar, Y. Takei, M. Shinohara, T. Kanazawa, E. Araki, and K. Suyehiro (2009), Seismic evidence for sharp lithosphere-asthenosphere boundaries of oceanic plates, *Science*, *324*(5926), 499–502, doi:10.1126/science.1169499.

Kennett, B. L. N., E. R. Engdahl, and R. Buland (1995), Constraints on seismic velocities in the Earth from traveltimes, *Geophys. J. Int.*, *122*(1), 108–124, doi:10.1111/j.1365-246X.1995.tb03540.x.

Kind, R., J. Ni, W. J. Zhao, J. X. Wu, X. H. Yuan, L. S. Zhao, E. Sandvol, C. Reese, J. Nabelek, and T. Hearn (1996), Evidence from earthquake data for a partially molten crustal layer in   southern Tibet, *Science*, *274*(5293), 1692–1694, doi:10.1126/science.274.5293.1692.

Kind, R. et al. (2002), Seismic Images of Crust and Upper Mantle Beneath Tibet: Evidence for Eurasian Plate Subduction, *Science*, *298*(5596), 1219–1221, doi:10.1126/science.1078115.

Kong, F., J. Wu, K. H. Liu, and S. S. Gao (2016), Crustal anisotropy and ductile flow beneath the eastern Tibetan Plateau and adjacent areas, *Earth Planet. Sci. Lett.*, *442*, 72–79, doi:10.1016/j.epsl.2016.03.003.

Le Fort, P. (1975). "Himalayas, the collided range: Present Knowledge of the continental arc". American Journal of Science 275A: 1–44

Lev, E., M. D. Long, and R. D. van der Hilst (2006), Seismic anisotropy in Eastern Tibet from shear wave splitting reveals changes in lithospheric deformation, *Earth Planet. Sci. Lett.*, *251*(3–4), 293–304, doi:10.1016/j.epsl.2006.09.018.

Levin, V. and J. Park (1997), P-SH conversions in a flat-layered medium with anisotropy of arbitrary orientation, *Geophys. J. Int.*, 131, 53-266.

Levin, V. and J. Park (1998), P-SH conversions in layered media with hexagonally symmetric anisotropy: A cookbook, *Pure Applied Geophys.,* 151, 669-697.

Levshin, A. L., and M. H. Ritzwoller (2001), Automated Detection, Extraction, and Measurement of Regional Surface Waves, *Pure Appl. Geophys.*, *158*(8), 1531–1545, doi:10.1007/PL00001233.

Li, H., W. Su, C.-Y. Wang, and Z. Huang (2009), Ambient noise Rayleigh wave tomography in western Sichuan and eastern Tibet, *Earth Planet. Sci. Lett.*, *282*(1–4), 201–211, doi:10.1016/j.epsl.2009.03.021.

Lin, F.-C., and M. H. Ritzwoller (2011), Helmholtz surface wave tomography for isotropic and azimuthally anisotropic structure, *Geophys. J. Int.*, *186*(3), 1104–1120, doi:10.1111/j.1365-246X.2011.05070.x.

Lin, F.-C., M. H. Ritzwoller, and R. Snieder (2009), Eikonal tomography: surface wave tomography by phase front tracking across a regional broad-band seismic array, *Geophys. J. Int.*, *177*(3), 1091–1110, doi:10.1111/j.1365-246X.2009.04105.x.

Lin, F.-C., M. H. Ritzwoller, Y. Yang, M. P. Moschetti, and M. J. Fouch (2011), Complex and variable crustal and uppermost mantle seismic anisotropy in the western United States, *Nat. Geosci.*, *4*(1), 55–61, doi:10.1038/ngeo1036.

Li, X., D. Wei, X. Yuan, R. Kind, P. Kumar, and H. Zhou (2011), Details of the Doublet Moho Structure beneath Lhasa, Tibet, Obtained by Comparison of P and S Receiver Functions,

Bull. Seismol. Soc. Am., *101*(3), 1259–1269, doi:10.1785/0120100163.

Mainprice, D., and A. Nicolas (1989), Development of shape and lattice preferred orientations: application to the seismic anisotropy of the lower crust, *J. Struct. Geol.*, *11*(1–2), 175–189, doi:10.1016/0191-8141(89)90042-4.

Marone, F., and B. Romanowicz (2007), The depth distribution of azimuthal anisotropy in the continental upper mantle, *Nature*, *447*(7141), 198–201, doi:10.1038/nature05742.

Marone, F., Y. Gung, and B. Romanowicz (2007), Three-dimensional radial anisotropic structure of the North American upper mantle from inversion of surface waveform data, *Geophys. J. Int.*, *171*(1), 206–222, doi:10.1111/j.1365-246X.2007.03465.x.

Mcnamara, D., T. Owens, P. Silver, and F. Wu (1994), Shear-Wave Anisotropy Beneath the Tibetan Plateau, *J. Geophys. Res.-Solid Earth*, *99*(B7), 13655–13665, doi:10.1029/93JB03406.

McNamara, D. E., W. R. Walter, T. J. Owens, and C. J. Ammon (1997), Upper mantle velocity structure beneath the Tibetan Plateau from Pn travel time tomography, *J. Geophys. Res. Solid Earth*, *102*(B1), 493–505, doi:10.1029/96JB02112.

Molnar, P., and P. Tapponnier (1975), Cenozoic Tectonics of Asia: Effects of a Continental Collision, *Science*, *189*(4201), 419–426, doi:10.1126/science.189.4201.419.

Montagner, J.-P., and N. Jobert (1988), Vectorial tomography—II. Application to the Indian Ocean, *Geophys. J.*, *94*(2), 309–344, doi:10.1111/j.1365-246X.1988.tb05904.x.

Montagner, J.-P., and H.-C. Nataf (1986), A simple method for inverting the azimuthal anisotropy of surface waves, *J. Geophys. Res.*, *91*(B1), 511, doi:10.1029/JB091iB01p00511.

Montagner, J.-P., and H.-C. Nataf (1988), Vectorial tomography—I. Theory, *Geophys. J.*, *94*(2), 295–307, doi:10.1111/j.1365-246X.1988.tb05903.x.

Montagner, J.-P., D.-A. Griot-Pommera, and J. Lavé (2000), How to relate body wave and surface wave anisotropy?, *J. Geophys. Res.*, *105*(B8), 19015–19,027, doi:10.1029/2000JB900015.

Moschetti, M. P., M. H. Ritzwoller, F. Lin, and Y. Yang (2010), Seismic evidence for widespread western-US deep-crustal deformation caused by extension, *Nature*, *464*(7290), 885–889, doi:10.1038/nature08951.

Nábělek, J., G. Hetényi, J. Vergne, S. Sapkota, B. Kafle, M. Jiang, H. Su, J. Chen, B.-S. Huang, and the H.-C. Team (2009), Underplating in the Himalaya-Tibet Collision Zone Revealed by the Hi-CLIMB Experiment, *Science*, *325*(5946), 1371–1374, doi:10.1126/science.1167719.

Nelson et al. (1996), Partially Molten Middle Crust Beneath Southern Tibet: Synthesis of Project
        INDEPTH Results, *Science*, *274*(5293), 1684–1688.

Nettles, M., and A. M. Dziewoński (2008), Radially anisotropic shear velocity structure of the
        upper mantle globally and beneath North America, *J. Geophys. Res.*, *113*, 27 PP.,
        doi:200810.1029/2006JB004819.

Okaya, D. A., and N. I. Christensen (2002), Anisotropic effects of non-axial seismic wave
        propagation in foliated crustal rocks, *Geophys. Res. Lett.*, *29*(11), 2–1–2–4,
        doi:10.1029/2001GL014285.

Ozacar, A. A., and G. Zandt (2004), Crustal seismic anisotropy in central Tibet: Implications for
        deformational style and flow in the crust, *Geophys. Res. Lett.*, *31*(23), L23601,
        doi:10.1029/2004GL021096.

Ozacar, A.A. and G. Zandt (2009), Crustal structure and seismic anisotropy near the San
        Andreas Fault at Parkfield, California, *Geophys. J. Int.,* 178, 1098–1104.

Pandey, S., X. Yuan, E. Debayle, F. Tilmann, K. Priestley, and X. Li (2015), Depth-variant
        azimuthal anisotropy in Tibet revealed by surface wave tomography, *Geophys. Res. Lett.*,
        42(11), 2015GL063921, doi:10.1002/2015GL063921.

Panning, M., and B. Romanowicz (2006), A three-dimensional radially anisotropic model of
        shear velocity in the whole mantle, *Geophys. J. Int.*, *167*(1), 361–379,
        doi:10.1111/j.1365-246X.2006.03100.x.

Rapine, R., F. Tilmann, M. West, J. Ni, and A. Rodgers (2003), Crustal structure of northern and
        southern Tibet from surface wave dispersion analysis, *J. Geophys. Res. Solid Earth*,
        108(B2), 2120, doi:10.1029/2001JB000445.

Royden, L. H., B. C. Burchfiel, R. W. King, E. Wang, Z. Chen, F. Shen, and Y. Liu (1997),
        Surface Deformation and Lower Crustal Flow in Eastern Tibet, *Science*, *276*(5313), 788–
        790, doi:10.1126/science.276.5313.788.

Rümpker, G., A. Kaviani and K. Latifi (2014), Ps-splitting analysis for multilayered anisotropic
        media by azimuthal stacking and layer stripping , *Geophys. J. Int.,* 199 (1), 146-163.
Schulte-Pelkum, V., and K. H. Mahan (2014a), A method for mapping crustal deformation and
        anisotropy with receiver functions and first results from USArray, *Earth Planet. Sci.
        Lett.*, *402*, 221–233, doi:10.1016/j.epsl.2014.01.050.

Schulte-Pelkum, V. and K. Mahan (2014b), Imaging faults and shear zones with receiver
        functions, *Pure Appl. Geophys.*, 171, 2967-2991.

Shao, T., S. Ji, S. Oya, K. Michibayashi, and Q. Wang (2016), Mica-dominated seismic
        properties of mid-crust beneath west Yunnan (China) and geodynamic implications,
        Tectonophysics, doi:10.1016/j.tecto.2016.04.024.

Shapiro, N. M., and M. Campillo (2004), Emergence of broadband Rayleigh waves from correlations of the ambient seismic noise, *Geophys. Res. Lett.*, *31*(7), n/a–n/a, doi:10.1029/2004GL019491.

Shapiro, N. M., and M. H. Ritzwoller (2002), Monte-Carlo inversion for a global shear-velocity model of the crust and upper mantle, *Geophys. J. Int.*, *151*(1), 88–105, doi:10.1046/j.1365-246X.2002.01742.x.

Shapiro, N. M., M. H. Ritzwoller, P. Molnar, and V. Levin (2004), Thinning and flow of Tibetan crust constrained by seismic anisotropy, *Science*, *305*(5681), 233–236, doi:10.1126/science.1098276.

Shen, W., and M. H. Ritzwoller (2016), Crustal and uppermost mantle structure beneath the United States, *J. Geophys. Res. Solid Earth*, 2016JB012887, doi:10.1002/2016JB012887.

Shen, W., M. H. Ritzwoller, and V. Schulte-Pelkum (2013a), A 3-D model of the crust and uppermost mantle beneath the Central and Western US by joint inversion of receiver functions and surface wave dispersion, *J. Geophys. Res. Solid Earth*, *118*(1), 262–276, doi:10.1029/2012JB009602.

Shen, W., M. H. Ritzwoller, and V. Schulte-Pelkum (2013b), Crustal and uppermost mantle structure in the central U.S. encompassing the Midcontinent Rift, *J. Geophys. Res. Solid Earth*, *118*(8), 4325–4344, doi:10.1002/jgrb.50321.

Shen, W., M. H. Ritzwoller, V. Schulte-Pelkum, and F.-C. Lin (2013c), Joint inversion of surface wave dispersion and receiver functions: a Bayesian Monte-Carlo approach, *Geophys. J. Int.*, *192*(2), 807–836, doi:10.1093/gji/ggs050.

Shen, W., M. H. Ritzwoller, D. Kang, Y. Kim, F.-C. Lin, J. Ning, W. Wang, Y. Zheng, and L. Zhou (2016), A seismic reference model for the crust and uppermost mantle beneath China from surface wave dispersion, *Geophys. J. Int.*, ggw175, doi:10.1093/gji/ggw175.

Simons, F. J., R. D. Van Der Hilst, J.-P. Montagner, and A. Zielhuis (2002), Multimode Rayleigh wave inversion for heterogeneity and azimuthal anisotropy of the Australian upper mantle, *Geophys. J. Int.*, *151*(3), 738–754, doi:10.1046/j.1365-246X.2002.01787.x.

Sloan, R. A., J. A. Jackson, D. McKenzie, and K. Priestley (2011), Earthquake depth distributions in central Asia, and their relations with lithosphere thickness, shortening and extension, *Geophys. J. Int.*, *185*(1), 1–29, doi:10.1111/j.1365-246X.2010.04882.x.

Smith, M. L., and F. A. Dahlen (1973), The azimuthal dependence of Love and Rayleigh wave propagation in a slightly anisotropic medium, *J. Geophys. Res.*, *78*(17), 3321–3333, doi:10.1029/JB078i017p03321.

Sol, S. et al. (2007), Geodynamics of the southeastern Tibetan Plateau from seismic anisotropy and geodesy, *Geology*, *35*(6), 563–566, doi:10.1130/G23408A.1.

Sun, Y., J. Liu, K. Zhou, B. Chen, and R. Guo (2015), Crustal structure and deformation under

the Longmenshan and its surroundings revealed by receiver function data, *Phys. Earth Planet. Inter.*, *244*, 11–22, doi:10.1016/j.pepi.2015.04.005.

Sun, X., X. Bao, M. Xu, D. Eaton, X. Song, L. Want, X. Ding, N. Mi, D. Yu, and H. Li (2015b), Crustal structure beneath SE Tibet from joint analysis of receiver functions and Rayleigh wave dispersion, *Geophys. Res. Lett.,* 41, 1479-1484.

Su, W., C. Wang, and Z. Huang (2008), Azimuthal anisotropy of Rayleigh waves beneath the Tibetan Plateau and adjacent areas, *Sci. China Ser. Earth Sci.*, *51*(12), 1717–1725, doi:10.1007/s11430-008-0137-x.

Tan, J., H. Li, X. Li, M. Zhou, L. Ouyang, S. Sun, and D. Zheng (2015), Radial anisotropy in the crust beneath the northeastern Tibetan Plateau from ambient noise tomography, *J. Earth Sci.*, *26*(6), 864–871, doi:10.1007/s12583-015-0543-x.

Tapponnier, P., X. Zhiqin, F. Roger, B. Meyer, N. Arnaud, G. Wittlinger, and Y. Jingsui (2001), Oblique Stepwise Rise and Growth of the Tibet Plateau, *Science*, *294*(5547), 1671–1677, doi:10.1126/science.105978.

Tatham, D. J., G. E. Lloyd, R. W. H. Butler, and M. Casey (2008), Amphibole and lower crustal seismic properties, *Earth Planet. Sci. Lett.*, *267*(1–2), 118–128, doi:10.1016/j.epsl.2007.11.042.

Thomsen, L., and D. L. Anderson (2015), Weak elastic anisotropy in global seismology, in *Geological Society of America Special Papers*, vol. 514, pp. 39–50, Geological Society of America.

Tian, Y., W. Shen, and M. H. Ritzwoller (2013), Crustal and uppermost mantle shear velocity structure adjacent to the Juan de Fuca Ridge from ambient seismic noise, *Geochem. Geophys. Geosystems*, *14*(8), 3221–3233, doi:10.1002/ggge.20206.

Wang, C.-Y., L. M. Flesch, P. G. Silver, L.-J. Chang, and W. W. Chan (2008), Evidence for mechanically coupled lithosphere in central Asia and resulting implications, *Geology*, *36*(5), 363–366, doi:10.1130/G24450A.1.

Weiss, T., S. Siegesmund, W. Rabbel, T. Bohlen, and M. Pohl (1999), Seismic Velocities and Anisotropy of the Lower Continental Crust: A Review, *Pure Appl. Geophys.*, *156*(1-2), 97–122, doi:10.1007/s000240050291.

Xie, J., M. H. Ritzwoller, W. Shen, Y. Yang, Y. Zheng, and L. Zhou (2013), Crustal radial anisotropy across Eastern Tibet and the Western Yangtze Craton, *J. Geophys. Res. Solid Earth*, *118*(8), 4226–4252, doi:10.1002/jgrb.50296.

Xie, J., M. H. Ritzwoller, S. J. Brownlee, and B. R. Hacker (2015), Inferring the oriented elastic tensor from surface wave observations: preliminary application across the western United States, *Geophys. J. Int.*, *201*(2), 996–1021, doi:10.1093/gji/ggv054.

Xu, L., S. Rondenay, and R. D. van der Hilst (2007), Structure of the crust beneath the

southeastern Tibetan Plateau from teleseismic receiver functions, *Phys. Earth Planet. Inter.*, *165*(3–4), 176–193, doi:10.1016/j.pepi.2007.09.002.

Yang, Y., M. H. Ritzwoller, Y. Zheng, W. Shen, A. L. Levshin, and Z. Xie (2012), A synoptic view of the distribution and connectivity of the mid-crustal low velocity zone beneath Tibet, *J. Geophys. Res.*, *117*, 20 PP., doi:201210.1029/2011JB008810.

Yao, H., C. Beghein, and R. D. van der Hilst (2008), Surface-wave array tomography in SE Tibet from ambient seismic noise and two-station analysis - II. Crustal and upper-mantle structure, *Geophys. J. Int.*, *173*, 205–219.

Yao, H., R. D. van der Hilst, and J.-P. Montagner (2010), Heterogeneity and anisotropy of the lithosphere of SE Tibet from surface wave array tomography, *J. Geophys. Res.*, *115*(B12), B12307, doi:10.1029/2009JB007142.

Yuan, H., B. Romanowicz, K. M. Fischer, and D. Abt (2011), 3-D shear wave radially and azimuthally anisotropic velocity model of the North American upper mantle, *Geophys. J. Int.*, *184*(3), 1237–1260, doi:10.1111/j.1365-246X.2010.04901.x.

Zhang, P.-Z., X. Wen, Z.-K. Shen, and J. Chen (2010), Oblique, High-Angle, Listric-Reverse Faulting and Associated Development of Strain: The Wenchuan Earthquake of May 12, 2008, Sichuan, China, *Annu. Rev. Earth Planet. Sci.*, *38*(1), 353–382, doi:10.1146/annurev-earth-040809-152602.

Zheng, Y., W. Shen, L. Zhou, Y. Yang, Z. Xie, and M. H. Ritzwoller (2011), Crust and uppermost mantle beneath the North China Craton, northeastern China, and the Sea of Japan from ambient noise tomography, *J. Geophys. Res. Solid Earth*, *116*(B12), B12312, doi:10.1029/2011JB008637.

Zhou, L., J. Xie, W. Shen, Y. Zheng, Y. Yang, H. Shi, and M. H. Ritzwoller (2012), The structure of the crust and uppermost mantle beneath South China from ambient noise and earthquake tomography, *Geophys. J. Int.*, *189*(3), 1565–1583, doi:10.1111/j.1365-246X.2012.05423.x.